Investigating the Terrible Triad Injury of the Elbow:

Expanding Knowledge using Advanced Computational Methods.

Inaugural Dissertation

zur

Erlangung des Doktorgrades

philosophiae doctor (PhD) in Health Sciences

der Medizinischen Fakultät

der Universität zu Köln

vorgelegt von

Stephanie Lucina Kahmann

aus Münster

2024

Investigating the Terrible Triad Injury of the Elbow:

Expanding Knowledge using Advanced Computational Methods.

Inaugural Dissertation

zur

Erlangung des Doktorgrades

philosophiae doctor (PhD) in Health Sciences

der Medizinischen Fakultät

der Universität zu Köln

vorgelegt von

Stephanie Lucina Kahmann

aus Münster

Betreuer	Prof. Dr. Kilian Wegmann
Gutachter	Prof. Dr. Harry van Lenthe
	Prof. Dr. Holger Grüll
	Prof. Dr. Maurice Balke
Datum der Mündlichen Prüfung	29.07.2024

Content

Acknowledgements

Javier: thank you for always being there for me, for understanding, for reflecting and noting, for cooking and taking care, for bringing in a second perspective and always having my best interest on mind. Thank you for challenging my way of thinking, and promoting my personal growth. Thank you for always being on my side and having my back. I love you.

Mama & Papa and Julius & Ann-Kathrin: Thank you for always being there, for always coming up with stupid jokes, kind words or whatever other helper was needed to raise the mood. I always felt supported, never pressured, always understood and never facing too high expectations. Thank you! I always knew that coming back home would mean time off, distance and relaxation and that is wonderful. I love you.

Viola, Nadja, Manu: Thanks for accompanying me through all ups and downs, for recalibrating my perspective and for many evenings of deviation, fun, consultation, philosophizing, wine tasting, whatever was necessary to get all of us through these funny times! I love you.

 Alex: thank you for your inspiration, for believing in me and for guiding me in the right direction. So many discussions in the office lead to fantastic ideas and to a broader view. I never would have started that journey without you and am grateful that you became a great friend after what started off as students with a similar field of interest. Thank you!

Abbreviations

Abbreviation	Definition
AI	Artificial Intelligence
CCC	Concordance Correlation Coefficient
CT	Computer Tomography
CI	Confidence Interval
DASH	Disability of the Arm, Shoulder and Hand
DIC	Digital Image Correlation
DL	Deep Learning
FEA	Finite Element Analysis
FEM	Finite Element Model
LCL	Lateral Collateral Ligament
LCLC	Lateral Collateral Ligament Complex
LUCL	Lateral Ulnar Collateral Ligament
MCL	Medial Collateral Ligament
MEPS	Mayo Elbow Performance Score
MRI	Magnet Resonance Imaging
PLER	Posterolateral External Rotation
PLIR	Posterolateral Internal Rotation
PMMA	Polymethyl methacrylate
PMS	Pressure Mapping Sensor
RMSE	Root Mean Squared Error
TTI	Terrible Triad Injury
UCL	Ulnar Collateral Ligament

Abstract

The terrible triad injury of the elbow consists of a dislocation, and fractures of the radius and the coronoid [1]. It is commonly accompanied by pain, instability of the joint and limited range of motion [2]. The outcome of the treatment of these injuries has improved with research over the last years and, in some publications, is considered not so terrible anymore [3]. Despite that, meta analyses showed that even with the research in the specific field, the outcome has not improved sufficiently and that, apart from good and excellent results, still moderate to poor outcomes are reported [4]. Therefore, this work aims to contribute to improving this situation by deepening the knowledge about the injury and by promoting research that may improve the clinical approaches in the treatment of the terrible triad injury.

There is still no consensus regarding the exact fracture mechanism of terrible triad injuries. In order to achieve deeper understanding of it, we designed a Finite Element Analysis [5]. Since no validated model of the entire elbow has been made available yet, we provide this groundwork: a validated simulation of the physiological elbow. The simulation parameters were adjusted to best match the experiment of its subject-specific biomechanical counterpart. These optimized parameters were then applied to the remaining 7 samples and compared to their experimental results. We found that the stiffness and the pressure distribution in the joint were predicted with moderate correlation on average. Further, the joint in which peak pressure was measured was predicted correctly in all 7 test cases. In future research, the fracture model can be based on this simulation

Apart from that, it is not yet well understood if the radial head fracture and the coronoid fracture reflect specific fracture patterns when they occur in the context of terrible triad injuries. In order to explore that, we automated parts of the formerly manual process in creating fracture heat maps with an algorithm [6]. We hypothesized that the algorithm performs the same task faster than the manual execution and that it shows no large deviation (< 5.0 mm) from the manually detected edges. The hypotheses were confirmed, as the algorithm was 23-times faster and showed a deviation of 2.5 ± 2.4 mm compared to the manual execution in proximal humerus fractures. Furthermore, fractures of the distal humerus, tibia plateau, scaphoid and acetabulum could be processed. Further research has to demonstrate applicability to the terrible triad injury. With these two research studies, the basis is created to gather clinically relevant data in the future, deepening the understanding of the terrible triad injury and, in the long term, improving the situation for patients.

Zusammenfassung

Die "terrible triad" (engl., schreckliche Dreiergruppe) Verletzung am Ellenbogen ist eine komplexe Dislokation mit Frakturen des Radiuskopfs und Coronoids [1]. Sie geht oft einher mit Schmerzen, Instabilität und eingeschränktem Bewegungsumfang [2]. Zwar hat sich das outcome nach Behandlung der Verletzung in den letzten Jahren verbessert und mittlerweile wird sogar teilweise postuliert, dass sie daher nicht mehr „terrible", also schrecklich, sei [3]. Allerdings haben Metastudien gezeigt, dass neben guten und exzellenten Ergebnissen auch immer noch mittelmäßige und schlechte auftreten [4]. Daher soll diese Arbeit dazu beitragen, das Wissen über die Verletzung zu vertiefen und wissenschaftliche Ergebnisse hervorzubringen, die die Behandlung verbessern können.

Noch immer gibt es keinen Konsens über den exakten Verletzungsablauf. Um das Verständnis zu vertiefen, haben wir eine Finite Elemente Analyse angefertigt [5]. Da noch kein validiertes Modell des ganzen Ellenbogens veröffentlicht wurde, stellen wir diese Grundlage auf: eine validierte Simulation des physiologischen Ellenbogens. Die Simulationsparameter wurden an die präparate-spezifischen experimentellen Parameter angepasst. Diese Parameter wurden dann auf die übrigen 7 Präparate angewendet und mit den experimentellen Ergebnissen verglichen. Dabei haben wir herausgefunden, dass die Steifigkeit und die Druckverteilung im Gelenk mit durchschnittlich moderater Korrelation vorausgesagt wurden. Dazu wurde die Druckspitze in allen 7 Versuchspräparaten im korrekten Gelenk vorhergesagt. Auf dieser Grundlage aufbauend kann in der Zukunft ein Frakturmodell des Ellenbogens entwickelt werden.

Des Weiteren ist noch nicht ganz erforscht, ob die Radiuskopf- und Coronoidfrakturen im Kontext der terrible triad Verletzung bestimmten Mustern folgen. Um das herauszufinden, haben wir einen Algorithmus entwickelt, der Teile der ehemals manuellen Ableitung von sogenannten Wahrscheinlichkeits-Heatmaps automatisiert [6]. Dabei haben wir die Hypothese aufgestellt, dass der Algorithmus schneller ist und keine großen Abweichungen (< 5,0 mm) im Vergleich zur manuellen Erkennung der Frakturkanten aufweist. Dies wurde bestätigt: der Algorithmus war 23 mal schneller und wies eine Abweichung von 2,5 ± 2,4 mm zur manuellen Ausführung am proximalen Humerus auf. Außerdem konnte der Algorithmus noch Frakturen des distalen Humerus, Tibia Plateau, Scaphoid und Acetabulum verarbeiten.

Mit diesen beiden Studien wurde eine Grundlage geschaffen, mit der klinisch relevante Daten erhoben werden können, die das Verständnis der terrible triad Verletzung vertiefen und langfristig die Situation für Patienten verbessern.

Thesis outline

The overall aim of the dissertation is to contribute to an improved outcome for patients with terrible triad injury. This complex dislocation is connoted with pain, limited function and instability of the joint, and it still leads to varying outcome [1]. **In chapter 1**, the reader is introduced to the common fracture situations and the most common group of patients. Further, the current state of the art regarding treatment of the injury as well as regarding biomechanical and clinical research on the injury are presented. Improving the poor outlook for patients is desirable and could be achieved with a better understanding of the injury [7]. We stepped into this direction by means of two computational approaches, which aim to deepen the knowledge of the fracture mechanism and of the fracture pattern, respectively.

On the one hand, a finite element model can provide valuable information regarding the fracture mechanism. Since models can only become clinically relevant when they are validated [8,9] and no validated model of the entire elbow has been made available yet [10,11], this preliminary goal must be achieved first. We contribute to this journey with a combined finite element model and biomechanical experiment of the physiological elbow that is mechanically well-controlled. **In chapter 2,** our study combining a biomechanical experiment and a finite element analysis of the human elbow is presented [5]. We hypothesized that the finite element model can predict the experimental contact pressure distribution, the stiffness, peak pressure and load share moderately to well and can predict the location of the peak pressure correctly (radio-humeral or humero-ulnar joint). To address these hypotheses, the finite element model includes both the radio-capitellar and the ulno-trochlear joint as both forearm columns take up a significant portion of the elbow contact force [12–15]. It is based on CT data of 8 cadaveric specimens and subjected to loads common during activities of daily living in order to obtain clinically relevant results. Several parameters of the model were studied in one specimen and the best matching result was propagated to the remaining seven models. This finite element workflow is combined with biomechanical experiments on their subject-specific cadaveric counterparts. Both approaches reflect on the pathomechanic position of the terrible triad injury: pronation and full extension. In the experimental model, the displacement under load and the joint pressure were measured. Eventually, the results of the finite element workflow were compared to the experimental data. Even though the simulation predicted the experimental contact pressure

distribution and the construct stiffness only with moderate correlation, the experimental peak pressure was predicted in the correct joint in all cases. The finite element model parameters as well as the experimental set up can still be improved in future research so that a validated finite element model of the elbow can be achieved.

On the other hand, the evaluation of CT scans can contribute to a thorough insight into fracture patterns, e.g. of terrible triad injuries. The partial automation of this process enables a time-efficient evaluation less dependent on the number of patients' CT scans. Therefore, we developed an algorithm that detects the edges of the fragments and superposes them, generating a heat map of fracture probabilities. With this reduction in manual labor, retrospective studies of CT scans can be facilitated, therefore more studies of the fracture patterns in terrible triad injuries can be published so that broader data will be available in the future. **In chapter 3,** this algorithm is described [6]. We hypothesized that our algorithm performs parts of the manual task with only little deviation (<5.0 mm) and faster than the equivalent manual execution. After the CT scans are segmented, and the fragments identified and reduced manually, the algorithm runs all steps towards the three-dimensional fracture probability heat map automatically. These steps comprise the transformation of the mesh of an intact bone onto that of the fractured bone, where all nodes corresponding to the separate fragments are identified. Then, the edges of the fragments can be detected in the mesh of the intact bone. This procedure is repeated for all fractured bones and the detected fracture edges are superposed in the intact bone mesh. As result, a three-dimensional heat map of fracture probabilities is created. We compared this automated approach to the former gold standard, the manual transmission of fracture lines from the fractured onto an intact sample. The algorithm showed acceptable results in precision and a considerably shorter processing time. Through the automation of the formerly time-intensive evaluation of CT scans of fragments, it is believed that more fracture evaluations will be published and therefore, a broader data basis is created to evaluate the fracture pattern of terrible triad injuries.

In chapter 4, the results of chapters 2 and 3 are discussed and their impact on the current state of science in the terrible triad injury assessed. The implications of these studies as well as the next steps in the journey towards improved outcomes for patients with terrible triad injuries are shown. Once a finite element model with improved parameters is evolved, based on our model and results, a fracture model can be implemented. This may allow for diverse simulations on terrible triad injuries, helping to evaluate the role of ligaments in the fracture mechanism and their stabilizing contribution in the treatment plan. Apart from that, research regarding

prostheses and pressure distributions in the joint in different situations of daily living can be carried out, based on our finite element model of the elbow.

Through the automation of the formerly manual fracture edge detection and heat map generation, it is believed that more fracture evaluations will be published. Therefore, a broader data basis is created to evaluate the fracture pattern of terrible triad injuries. This includes promoting smaller studies from local institutions, as well as increasing the cohort in studies by larger, specialized institutions. From this facilitation, research not only on terrible triad injury but on a broad variety of fractures may benefit since the algorithm proved valuable for fractures in bones of different general shapes and sizes. Concluding, the role of the publications in progressing the research on terrible triad injuries is evaluated.

Chapter 1

Introduction: The terrible triad injury of the elbow

The terrible triad injury of the elbow

Definition

A terrible triad injury (TTI) of the elbow consists of fractures of the radial head and the coronoid and of a dislocation of the elbow. It was first mentioned as such by Hotchkiss et al. in 1996 due to its historically poor outcome [1] (Figure 1).
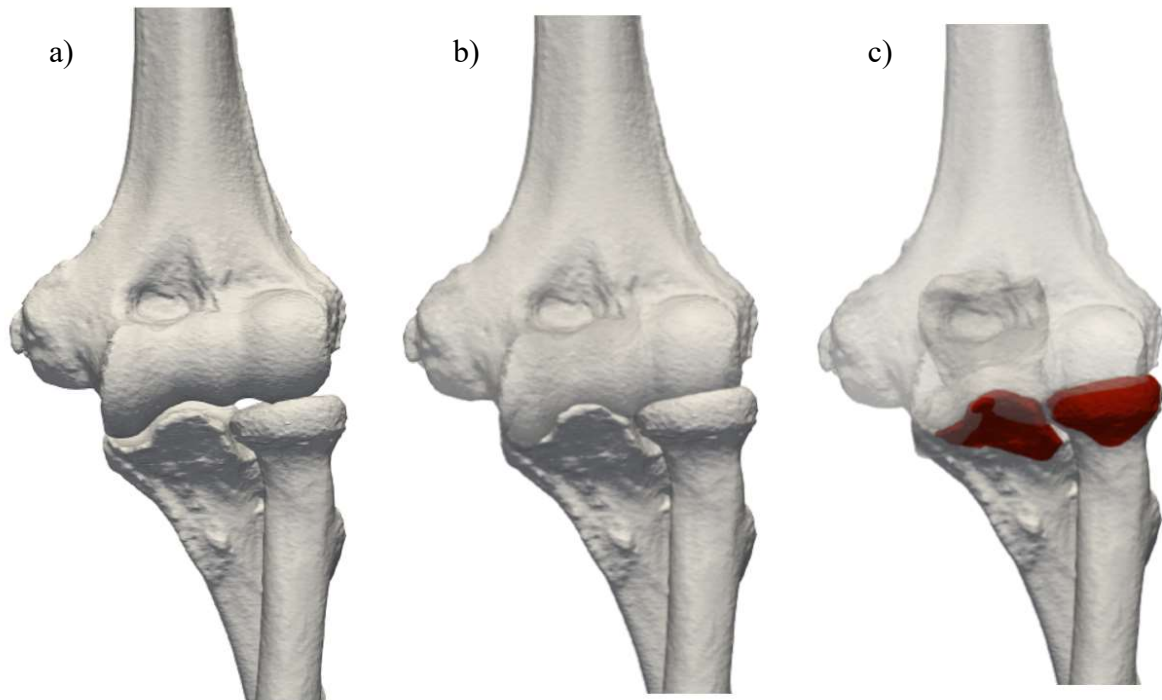
Figure 1a) The forearm and the humerus are still intact. b) During the fracture mechanism, the joint is compressed, so that c) the joint displaces and the coronoid and radial head fracture.

This fracture is particularly critical since both axial columns of the elbow are affected: the radio-humeral and the ulno-humeral joints. Frequently, the stabilizing lateral collateral ligament (LCL) complex is impacted as well [2] and, in 50-60% of the TTI cases, so is the medial collateral ligament (MCL) [16]. These factors are prone to impact the joint stability [17]. The injury commonly occurs in patients of relatively young age (mean 45 years) [18]. It is evoked by high impact, e.g. in traffic accidents, in falling accidents of different heights or during sports [19,20]. The patients are predominantly male (58 %) [4]. Apart from instability of the elbow, such a severe injury commonly causes stiffness, development of arthrosis and pain [1]. The increasing significance can be derived from the fact that in the same book series in the 2015 edition, already several sections were dedicated to the terrible triad injury [21].

State of the Art

Regarding the treatment, recently relevant biomechanical investigations and retrospective clinical studies have been published, evaluating the short- and long-term outcomes of different therapeutic approaches [3,22,23]. In particular, most studies investigated surgery protocols including different combinations of addressing the coronoid and radial head fractures, the MCL, LCL or the anterior capsule.

A study published by Pugh et al. included 36 patients and reported outcomes after surgery which consisted of repair of coronoid fracture, refixation/replacement of the radial head, and where possible, repair of the elbow capsule and of the LCL. In some cases, it was necessary to repair the MCL or apply an external fixator to restore joint stability. With this protocol, the mean Mayo elbow performance score (MEPS) of 88 could be achieved [24]. This is in line with other publications as they suggest that repairing the LCL complex (LCLC) prevents persistent elbow instability after TTI [25,26]. Similarly, Gupta et al. investigated the results of a standardized surgical protocol, consisting of radial head repair/replacement, coronoid refixation and LCL refixation. If the joint was still unstable intraoperatively, the MCL was refixed as well. At latest after secondary surgery for cases with heterotopic ossification, all patients had ranges of motion close to those required for activities of daily living [27].

In contrast, a more conservative approach was described by Papatheodorou et al. in a case series with 14 patients, who had coronoid fractures of the Regan Morrey type I or II. These fractures were not treated operatively; only the radial heads and LUCL were refixated or replaced. Intraoperative stability was confirmed with fluoroscopy, without fixation of the anterior capsule or the MCL. No instability was detected in this small cohort, nor was reoperation necessary, and in 13 out of 14 patients the range of motion allowed for performance of activities of daily living [28]. In a study by Ring et al., out of 11 observed cases only 4 showed satisfactory results regarding range of motion for activities of daily living. These were treated with refixed or retained radial head, and two with repair of the LCL. The authors emphasize that restoring stability of the joint is crucial in treatment of TTI, which is achieved through reconstruction of the radio-humeral joint and the LCL, and the coronoid if necessary [29].

Jung et al. agree with Ring et al. regarding the primary aim of surgery being to reestablish stability of the elbow joint. In their study, they investigated risk factors for the success of this goal with 76 patients, divided into the "recurrent instability" (15) or the "concentric stability" (61) group. Factors promoting instability are high energy trauma, comminuted radial head

fractures, injury of the MCL and not addressing the coronoid fracture. This point contradicts the findings by Ring et al., who achieved satisfactory results in four patients without addressing the coronoid. It was further found that the time between injury and surgery plays a role in the outcome of the treatment [30]. This was also investigated by Lindenhovius et al. In their study, 18 patients were operated in up to 14 days after injury with refixation of the coronoid, of the LCL and refixation or replacement of the radial head. In parallel, 14 patients were treated 21 days or later after injury and after initial treatment. In this group, 13 patients underwent radial head replacement, and the coronoid fracture was refixed in 9, the LCL was addressed in 13. Even though the range of motion improves with earlier surgery, as suggested by Jung et al., the outcome regarding stability and strength was similar in both groups [31].

Hou et al. addressed the coronoid process using a plate, refixed or replaced the radial head and reattached the LCL but not the MCL [20]. This approach is similar to that described by Lindenhovius et al. for the early operated group, neither addressing the MCL. With a MEPS of 83 and a disability of the arm, shoulder and hand (DASH) score of 22 in Hou et al. compared to 88 and 18 in Lindenhovius et al., the latter reported better results. The differences in outcome while applying a similar surgery protocol are an example of individual differences amongst patients.

Similar results regarding the MEPS were observed by Chemama et al. In a retrospective study with 23 elbows, 17 were treated addressing the radial head with refixation or replacement, 10 refixing the coronoid fracture and, in all cases all ligaments were reconstructed. Overall, good outcomes were achieved with this approach. In line with the findings of Jung et al., they stated that Mason Type III (comminuted) fractures of the radial head pose a risk factor for poor outcome [32]. Similarly, Jeong et al. repaired both fractured bones as well as the LUCL and, if injured, also the MCL. This procedure led to satisfactory results in terms of range of motion as well as MEPS. Elbow stability was achieved in all 13 observed cases with a mean follow-up time of 18 months [33].

Chen et al. ran a meta-analysis of studies comparing the repair to the replacement of fractured radial heads. In the cohort, most fractures were Mason type II or III. As outcomes, the DASH score and MEPS were considered. Fewer complications were associated with replacement than with repair of the radial head [34]. In two studies encompassed in this meta-analysis, the authors reported that the radial head was replaced when fractured into 4 or more fragments [35] and that the effort to repair was higher in younger patients [36]. Despite applying the replacement

approach in clinically more critical cases - the fracture being more complicated and the patients older - the replacement approach led to better overall results. Apart from that, the included studies had different protocols regarding the MCL. In Watters et al., the MCL was repaired when necessary for stability in 5 out of 39 cases [35], in Jeong et al. whenever it was teared [33], and in Leigh and Ball and Yan et al. it was not addressed [36,37]. These differences in surgical approach could distort the results derived in the meta-analysis.

Chen et al. report that compared to the last systematic review with publications up to 2009, the share of patients with good to excellent outcomes has "maintained, rather than increased". They state that continued improvement of the surgery protocols "will hopefully decrease the proportion of patients who experience fair to poor outcomes" [4]. Common complications of surgeries for terrible triad injuries were investigated based on 16 studies with a total of 312 patients. Overall, more than 20 % of these patients required reoperation, the most common reasons were unsatisfactory refixation or replacement, joint stiffness or instability and ulnar neuropathy [4].

With a conservative approach, surgical complications can be circumvented. In a study of Najd Mazhar et al., 14 out of 63 patients met specific criteria for nonsurgical treatment. Amongst others, these included a defined active range of motion that can be achieved pain-free, fractures of radius and ulna not requiring surgery and a stable joint. The patients included in this study had radial head fractures of the Regan-Morrey types I or II and coronoid fractures of the Mason type I or II. Even though the resulting MEPS and DASH score were acceptable, the range of motion in pronation/supination was limited. Therefore, they propose that only patients meeting even stricter criteria are suited for the conservative approach [19]. Similar results were reported by Chan et al. [38].

The role of the anterior capsule in the context of the TTI is still unclear. It was stated by Pugh and McKee that its repair could "significantly improve stability" of the elbow [39]. Contrarily, Antoni et al. found in a retrospective study with 30 patients that repair of the anterior capsule did not improve the clinical or radiographical outcome [40]. A middle way for the dispute was created by Papatheodorou, who stated that the capsule does not require repair in case the coronoid fracture was not too severe [28]. This could imply that repair of the anterior capsule is required only if the coronoid fracture is severe. Even though Fern et al. focused their study on the varus stability and did not investigate overall elbow stability, they found that larger

defects in the coronoid pose a strong risk of instability whereas minor defects can be compensated by addressing the LCL or the radial head [41].

All published studies on the terrible triad injury have led to an improved situation for patients. Even though the optimal surgery protocol is still not determined, a scoping review by Stambulic et al. showed that the average MEPS was 90, corresponding to excellent results, and therefore state that terrible triad injuries were "no longer terrible!" [3].

Regarding the fracture mechanism, in the original source it was assumed that a fall on the outstretched elbow in supination is the pathomechanic position for terrible triad injuries [1]. Re-investigating that, a study by Fitzpatrick et al. in 2012 thoroughly examined the probable fracture position with a biomechanical cadaver study. They found that in 6 out of 7 cases, samples in full pronation showed a terrible triad fracture pattern - significantly more frequently than in supination. During fracturing in pronation, external rotation of the ulna tended to tear the lateral ligaments and internal rotation the medial ligaments [42]. In a study by our research group, 13 cadaveric specimens were fractured in pronation and extension. The influence of added valgus load was investigated, and it was found that it did not lead to a more reliable observation of terrible triad fractures than with a mere axial impact: 7 out of 7 samples without and 5 out of 6 with valgus load showed a terrible triad fracture. The remaining sample had a radial head fracture and a dislocation but instead of the coronoid, the medial humerus fractured [43].

Extending the findings of affected ligaments from Fitzpatrick et al, Rhyou et al. carried out a retrospective study based on x-rays and MRI images of 40 patients with terrible triad injuries. In the most common injury pattern, the posterolateral displacement and external rotation (PLER) of the forearm, the LCLC and extensor muscles were torn by distraction in all, whereas the UCL was spared in some cases. This could suggest that identification of posterolateral displacement of the forearm in the x-ray should raise particular awareness regarding accompanying LCLC rupture and extensor muscle tear; inclusion of the UCL is probable [44].

Another approach investigating contact mechanics of the elbow are finite element models. Wake et al developed a workflow to examine the fracture-dislocation of the coronoid and olecranon, combining experimental and computational data. Even though the study included a large experimental cohort, the finite element analysis neglected the radius and could therefore not serve as a basis for the investigation of the terrible triad injury [45]. In addition, both this study and one published by Merz et al. reduced the mechanical problem to a two-dimensional

finite element analysis, neglecting the medial-lateral joint orientation [46]. In contrast, both Renani et al. and Langohr et al., developed three-dimensional finite element models to investigate the elbow joint mechanics. However, Langohr et al. neglected the ulno-trochlear and Renani et al. the radio-capitellar joint of the elbow, focusing on their specific research question only [47,48]. Therefore, neither of these models was suited as groundwork to simulate the terrible triad injury fracture mechanics.

Apart from this approach, the fracture mechanics of the terrible triad injury can be investigated retrospectively, evaluating the fracture pattern in CT scans. Mellema et al. examined if particular fracture patterns correlate with overall fracture types. They found that this is indeed the case for coronoid fractures but not for radial head fractures in terrible triad injuries [49,50]. This might suggest that information about the coronoid fracture could provide information of impacted soft tissue and the radial head if the fracture pattern can be identified clearly.

In summary, up to now research focused on the retrospective analysis of patients with terrible triad injuries and their long-term outcome, on biomechanical models reproducing the fracture pattern. Further, several finite element analyses on partial elbows and manual retrospective statistical analyses of CT scans were published, which served as a basis for our research.

Chapter 2

A combined experimental and finite element analysis of the human elbow under loads of daily living

A combined experimental and finite element analysis of the human elbow under loads of daily living

Stephanie L. Kahmann [a], *, Amelie Sas [b], Nils Große Hokamp [c], G. Harry van Lenthe [b], Lars-Peter Müller [a], Kilian Wegmann [a]

[a] University of Cologne, Faculty of Medicine and University Hospital Cologne, Center for Orthopedic and Trauma Surgery, Kerpener Str. 62, Cologne 50937, Germany

[b] Biomechanics section, Dept. of Mechanical Engineering, KU Leuven, Belgium

[c] University of Cologne, Faculty of Medicine and University Hospital Cologne, Institute for Diagnostic and Interventional Radiology

*Corresponding author

Adapted from:

2.1   Introduction

The elbow joint provides crucial mobility and functionality for activities of daily living [51]. Severe injuries, such as the terrible triad lesion of the elbow, can cause stiffness and severe pain [1,28,31,52], which negatively impact the patients' independence and dignity immediately. Therefore, profound knowledge of the intact state may help improve the treatment [7] and finite element models (FEM) are an established tool to improve understanding of joint biomechanics [53]. This computational approach has been applied to a great extent in the hip [54–56] and knee research [57–59]; however, the elbow is not yet well represented.

To be able to draw clinically meaningful results from finite element models of the elbow, these must be tested under realistic conditions, including realistic loads and adequate representation of all relevant structures. Common loads in the ulno-trochlear and radio-capitellar joints range up to 1600 N and 800 N during occupational activities [60]. The elbow joint is regularly subjected to forces between 0.5 to 3 times body weight in activities of daily living, ranging up to 2 times body weight [61,62]. According to the literature, 54-67 % of the pressure is transmitted through the radius in elbow extension [12–15]. The distribution of load transfer directly impacts the pressure distribution within the joint, which is an important evaluation criterion in the development of prosthesis and treatment options [48].

Thus far, published models of the elbow have been validated up to 200 N [10]. In view of the actual loads, this is very low. Furthermore, this model neglected a detailed description of the ulna. Willing et al. have presented an elbow model including both forearm bones [11]. Their study focused on the cartilage contact mechanics, and, for their purpose, 80 N of load sufficed. However, this range does not fulfill the wide range of loads in the activities of daily living. Hence, among the published elbow models, we identified the lack of a model that includes both the radio-capitellar and the ulno-trochlear joint, and that is subjected to realistic loads.

We aim to fill this gap with a subject-specific finite element workflow with parameters that are optimized for one specimen and subsequently tested in a test-cohort of seven specimens of the native elbow joint. We compare the experimental and simulated locations of peak pressure and the overall pressure distribution, being relevant parameters for correct prostheses design, and the stiffness as a parameter for the deformation occurring in the joint. Furthermore, we compare the contact areas, peak pressure magnitudes and percentage of load share on the radius.

2.2   Materials and Method

Preparation

Eight cadaveric arms from 4 donors (1 female and 3 male), with an average age of 78 (range 62-89) years were used. Ethical approval was granted under the number VT 21-1514_1 prior to the study.

Before in-vitro testing, the humerus was dissected 12 cm proximal of the joint line and the forearm bones 7 cm distal of it, which were the highest common lengths of all samples. The specimens were potted into custom-made aluminum cylinders with polymethyl methacrylate (PMMA, Technovit, Kulzer GmbH, Wehrheim, Germany) in full extension and 60° pronation. The height of the fixation was marked at 3 cm. Each specimen was equipped with 6 tantalum beads (0.8 mm, x-medics, Frederiksberg, Denmark) of which two were inserted in the proximal shaft, one in the medial epicondyle of the humerus, one in the proximal end of the olecranon and two in the radial shaft. Then, cross sectional computed tomography (CT) images of the specimens were obtained in the anatomic position of the experiment, using a clinical CT system with a modified protocol (Philips IQon, Philips Healthcare, Best, The Netherlands). Helical CT image acquisition was performed using 120 kVp, 250 mAs and a pitch of 0.235. Images were reconstructed using a hybrid-iterative reconstruction algorithm with a sharp kernel (iDose4 and C, Philips Healthcare, Best, The Netherlands). Images were reconstructed in a slice thickness of 0.67 mm without increment. Given a matrix of 1024x1024 and the field-of-view of 350x350 mm^2, in plane resolution was 0.34x0.34 mm^2.
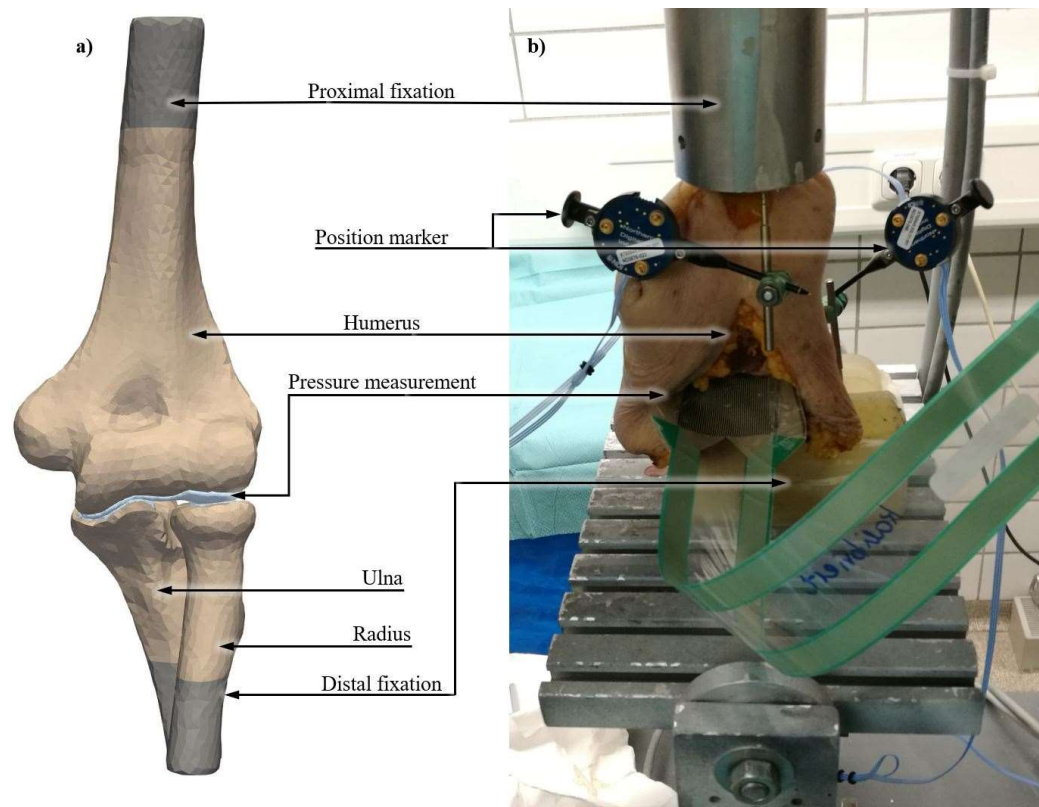
Figure 2: The set-up of the simulation (a) and experiment (b) are analogous to each other. The proximal fixation of the simulation is derived from the resin height in the aluminum pot and its displacement, measured with the position markers, is applied as boundary condition to the simulation. In both cases, the humerus presses axially on the pressure measurement: measured in the cartilage (a) and the pressure mapping sensor (b). In the simulation (a), the ulna and radius are well visible whereas the soft tissue and the pressure mapping sensor obstruct the view in (b). The distal fixation of the simulation (a) corresponds in height and degrees of freedom to the resin, fixated to the bottom table with screws (b).

A pressure mapping sensor (PMS, Model 5040; Tekscan, Inc., Boston, MA) with spatial and temporal resolutions of 1.03 mm² and 10 Hz was preconditioned and calibrated under experiment-like conditions. The PMS was placed between two silicon layers, lubricated with machine oil, on a flat table and a stamp, both made of steel, in a material testing machine (error ±1 N, Modell Z010, Zwick Roell, Ulm, Germany) to mimic the cartilage covered bone. During the calibration and the experiment, the PMS was protected from the moist environment by a Tegaderm Film (3M Deutschland GmbH, Neuss, Germany) [47,63]. The conditioning loads ranged up to 110% of the highest expected pressure (1.27 MPa), estimated based on a previous study [12]. A custom-adapted second order polynomial calibration curve was found to show the lowest root mean squared error (RMSE 0.05 MPa), as suggested by Brimacombe et al. [64]. Several parameters were based on preliminary studies in one specimen and the best matching set was applied to the remaining 7 specimens in the comparison cohort.

Experiment

The potted specimens were fixed in the material testing machine (Z010, Zwick Roell, Ulm, Germany) to the bottom table with screws and press fitted to the top pot, which was itself rigidly attached to the actuator (Figure 2b). The specimens were placed in full extension and 60° pronation. This position was chosen as a well-controlled set-up. The skin was incised axially at the ventral center of the elbow over 7 cm. Further blunt dissection, moving the muscles to the sides, giving unobstructed view on the ventral capsule, which was cut transversally along the joint gap, allowed for insertion of the PMS. Through two dorsal puncture incisions medially and laterally of the olecranon, two clamps grabbed the PMS and prevented it from shifting during force application. Thus, it was ensured that the PMS covered the whole joint. In the resins around the humerus and the forearm, two position markers (Smart Cluster Marker, Optotrak, Northern Digital Inc., Waterloo, Ontario, Canada) were mounted. The position markers measured the vertical displacements with a maximum error of 0.005 mm.

Under a preload of 10 N, the positions of the tantalum beads were measured with an optical tracking device (Four Marker Rigid Body, Optotrak Certus, Northern Digital Inc., Waterloo, Ontario, Canada). These positions were the basis for the fine registration in the simulation and were measured with an accuracy of 0.03 mm.

The humeri were loaded axially with a rate of 0.6 mm/min. A load cycling 30 times between 10 and 100 N served as the preconditioning. This was followed by the test protocol, starting at 10 N, increasing to 100 N and from there in 100 N increments up to 1000 N. Subsequently, the load was decreased in the same manner back to 10 N. At each step of the test protocol, the position was held for 60 s. Meanwhile, the pressure and the displacements were recorded with the PMS and the position markers, allowing to monitor the stiffness, defined as force over displacement. The whole protocol was repeated three times per specimen.

Simulation

All CT scans were segmented semi-automatically using the same scripted Mimics functions (smoothing with a smoothing factor of 0.4 for three iterations, eroding and dilating with the size of 1 pixel in relation to the 26 connected pixels, wrapping with the default values (detail 0.3906 and gap 0.195313), and then manual correction of intersections, Mimics Version 22.0, Materialise, Leuven, Belgium). For correct alignment, the geometries of the bones were registered to their respective positions in the experimental set-up by transforming the positions

of the tantalum beads from the CT scan to the experimentally measured position in a CAD Software (3-matic Version 12.0, Materialise, Leuven, Belgium). This way, the coordinate systems from the measurement in the experiments matched those in the simulations. A preliminary study demonstrated the necessity of this measure to reflect the joint alignment correctly (1° axial rotation of the humerus changed the peak pressure by 2%). Once the bones were aligned, the cartilage geometries on the humerus, ulna and radius were created based on the joint surfaces. The constant cartilage thickness was manually increased up to contact with the opposing cartilages and ranged from 0.7 to 1.1 mm among all specimens.

In the next step, the mesh size was assigned. In a mesh sensitivity study, an edge length of 1 mm in the region of interest covering 25 mm proximal and distal of the joint lines proved to be the appropriate balance of precision and runtime (<6% deviation in peak contact pressure compared to 0.9 and 1.1 mm edge lengths). The meshes outside the region of interest had an average edge length of 3 mm. Regular tetrahedral elements (C3D10) were used, due to bending in a preliminary study and for accurate peak pressures in penalty-ruled contact (Abaqus Version 2017, Simulia, Dassault Systèmes, Vélizy-Villacoublay, France) [65].

Young's Moduli were assigned dependent on the density, according to the linear elastic portion of the Keyak bone fracture model [66]. Therefore, the density was discretized in 10 bins for each the spongious and the cortical bone [67]. More than 99% of all elements were assigned a Young's Modulus of 2-16,389 MPa. The cartilage material properties were based on a preliminary analysis. The Young's modulus was iteratively optimized approximating the experimentally measured stiffness with a fixed Poisson's ratio of 0.4 [10]. Within the tested range of 4 to 16 MPa, the 6 MPa case was found to be the best match. It was compared to Neo-Hookean material properties [11] in the exemplary load cases of 100 N and 1000 N. This property had only little effect on the stiffness and pressure distribution at a cost of longer computation time in the case of 100 N, which is in line with the finding of Kim and Miller [10], and did not converge at 1000 N. Therefore, the linear elastic model was chosen.

The cartilages were tied to their respective bones, and frictionless tangential contact was assigned within the joint [47]. In normal direction, the penalty stiffness increased linearly from $K_{initial} = E_{element}$ at an overclosure $e = 0.01g_0$ up to $K_{final} = 100 * E_{element}$ at $d = 0.03g_0$ with g_0 being the faceted element length [11].

The distal ends of both forearm bones were fixated in all six degrees of freedom up to the individual height of the resin, derived from the CT scans (Figure 2a). Similarly, the proximal

end of the humerus was restricted in transverse translation and rotations, only allowed to displace in axial direction. These displacements were governed by the subject-specifically measured displacements of the experiments using the optical tracking markers. This was found to be more sensitive than applying the load in a parameter sensitivity study: changing the assigned displacement by 0.1 mm (experimental error $\pm$ 0.005 mm), the force varied by around 70 N. When changing the applied load by 1 N (experimental error $\pm$ 1 N), no change in displacement was detectable. Therefore, the less sensitive displacement was chosen as input and the more sensitive reaction force as comparison parameter. The model stiffness is determined by the resulting forces over the applied displacements.
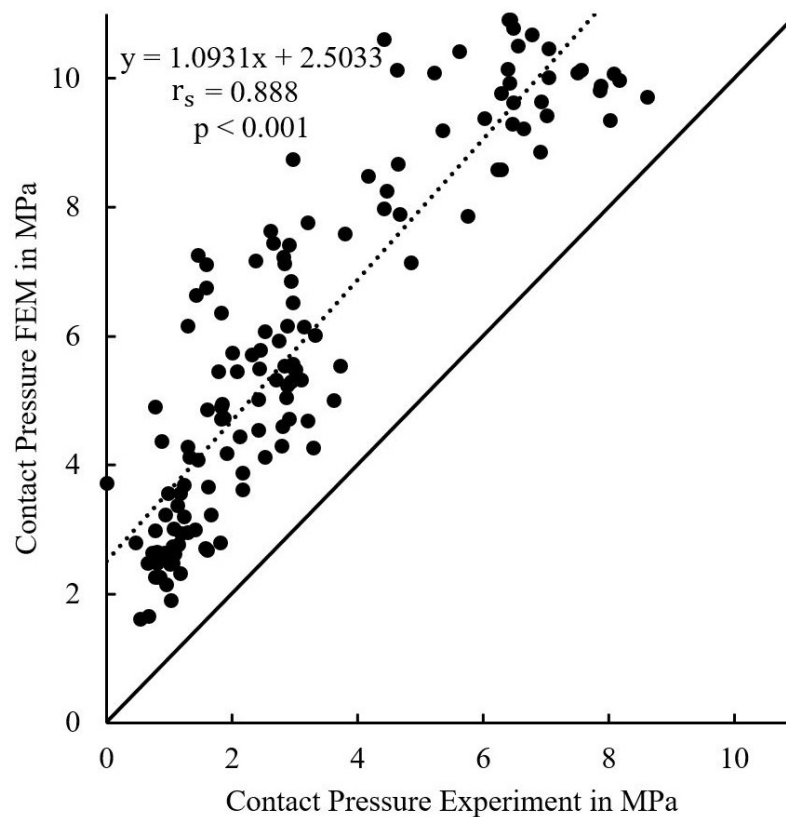
Figure 3: A subject-specific correlation of the simulated over the measured full-field pressure distribution with 137 local measurements is shown as an example. The finite element nodal output was averaged around the pressure mapping pixel output. Perfect agreement would be represented by a slope of 1, an intercept of 0 and a correlation R^2 of 1.

Data Processing and Statistical Evaluation

The experimental and simulated contact pressures were compared in a full-field approach. Therefore, the nodal joint contact pressure of the finite element analysis and moving average (3x3 matrix) filtered pressure mapping data were registered. That was achieved by projecting the 3-dimensional finite element geometry of the contact area onto the plane of the pressure

mapping sensor and normalizing both datasets to an area of the dimensions [0 1], both in the medial-lateral and ventral-dorsal directions. Using a published validation tool [68], the higher resolved simulation output was averaged around the lower resolved pressure mapping output.

For the comparison of the peak pressure locations, the computational and experimental coordinates were registered and normalized in the same way as for the full-field pressure comparison. But, instead of comparing the pressure values, the coordinates of the respective peak pressures were extracted and with them the identification of the contact joint (radial or ulnar).
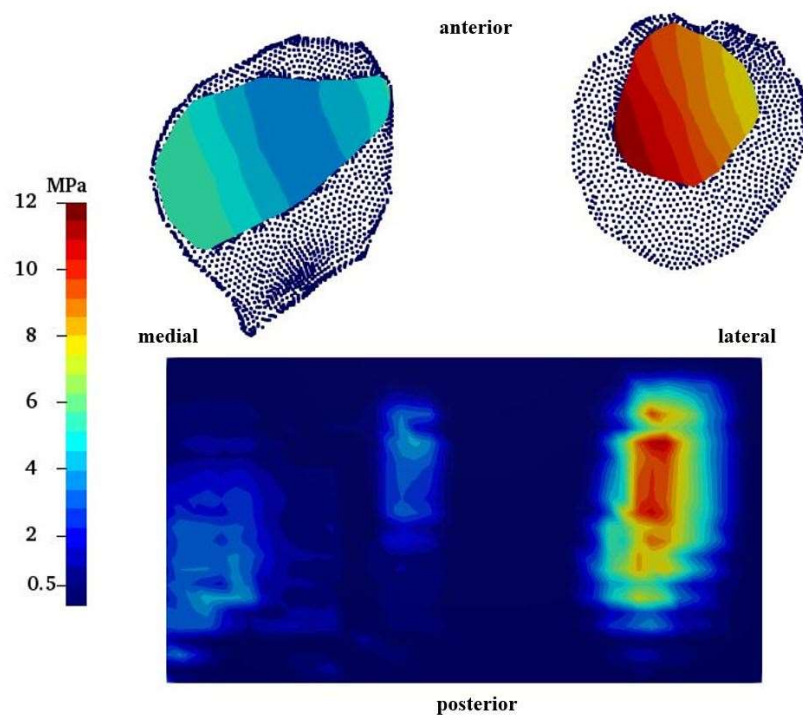

Figure 4: A comparison of the pressure distributions from simulation (top) and experiment (bottom), showing a similar distribution in a right arm as an example. The blue dots of the simulation indicate unloaded nodes of the cartilages, similar to the blue background of the pressure mapping.
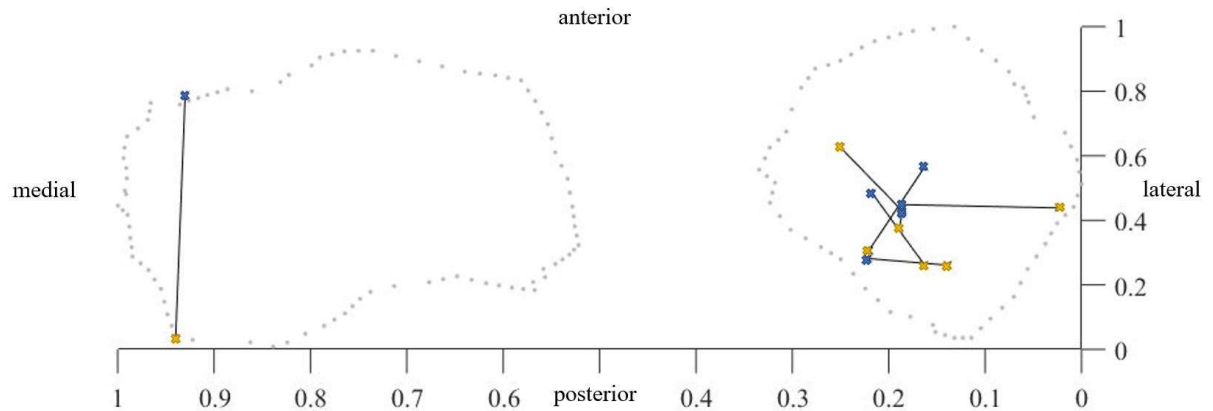
Figure 5: The peak pressure locations both predicted (yellow) and measured (blue), indicated by crosses and the subject-specifically corresponding ones connected with a line, projected into a right sample. All peak pressures were found in the correct joint: 6 in the radius and one in the ulna.

The experimentally measured displacements were partially affected by a non-congruency of the joints at lower loads, apparent in a contact area that was unphysiologically low (on average below 50% at the radius). This led to non-linear stiffness in the simulation. To prevent this error from propagating, we linearized the force-displacement diagram based on the load cases higher than 400 N, extrapolated the missing data and shifted the inception to the point of origin. In cases 2 and 6, no contact was detected in the humero-radial joint up to 300 N and 400 N, respectively, which strongly impacted the corresponding displacements. Therefore, these values were excluded from evaluation.

Statistical evaluation was performed using SPSS (IBM SPSS Statistics Version 28, IBM, Armonk, NY, USA). All tests for normal distribution were carried out using the Shapiro-Wilk test. Correlations over all samples were tested using Lin's concordance correlation coefficient (Lin's CCC) and subject-specific correlations using Spearman's rho. The significance level for all tests was defined at $p<0.05$. The 95 % confidence interval (CI) of the simulated force (Figure 7a) was calculated as a first-order normal approximation [69], showing the range, in which a population value would lie with a probability of 95 %, based on the samples included in this study.

2.3 Results

The computational and experimental pressure distributions of each subject correlated with an average Spearman's rho of 0.496 (range 0.260-0.888, p < 0.01) (Figure 3). In both distributions of Figure 4, the medial side of the radius and the medial and lateral side of the ulna showed high pressure with elliptical contact areas. Regarding the contact area, the model correlated poorly to moderately with the experiment (Table 1).

Table 1: Parameters are evaluated at 1000 N load, here shown as mean (± standard deviation). Lin's correlation concordance coefficient (Lins's CCC ± 95 % confidence interval) indicates the correlation between the experimental and the simulated results.

Parameter	Experiment	FEA	Lin's CCC
Mean peak pressure in MPa	10.1 (± 3.3)	13.7 (± 7.8)	0.333 (± 0.397)
Mean load share in % on radius	57.2 (± 18.2)	51.7 (± 15.7)	0.655 (± 0.467)
Mean contact area in mm²	395.4 (± 68.8)	225.4 (± 63.4)	0.152 (± 0.198)

Furthermore, it was predicted correctly for all 7 comparison specimens, in which joint the peak pressure occurred (Figure 5). In 6 cases it was detected in the radio-humeral joint, one in the humero-ulnar joint. The average magnitude of this peak pressure among all specimens was 10.1 ± 3.3 MPa (mean ± standard deviation) in the experiments and 13.7 ± 7.8 MPa in the FEM (Figure 6). The predicted and measured peak pressures of both joint contacts separately at 1000 N correlated with Lin's CCC of 0.333 ± 0.397 (Table 1). The experimental peak pressures before and after the waiting period of 60 s differed less than 0.04 MPa; the repetition showed an average standard deviation of 0.1 MPa with no apparent trend. Further, we found that neither the ascending nor the descending order of load cases affected the measured parameters.

$$y = 1.2534x + 1.0534$$
$$R^2 = 0.2826$$
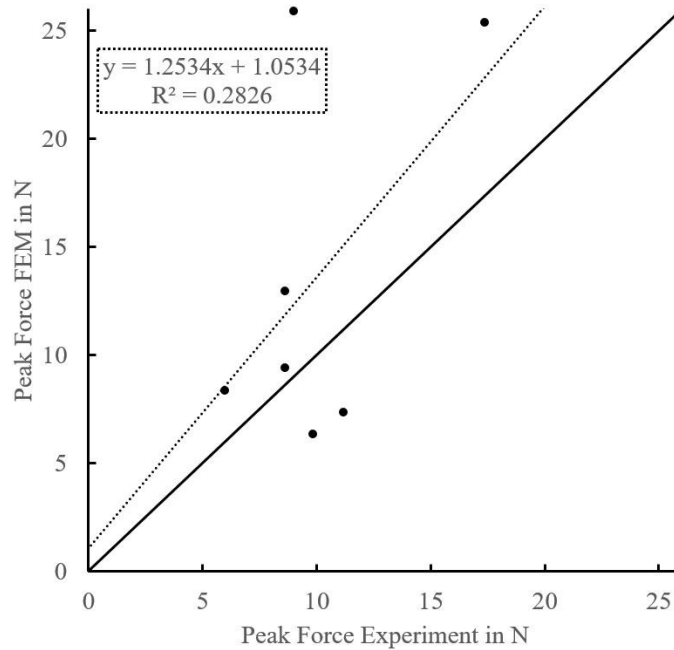
Figure 6: The peak pressure magnitudes of the simulation are shown over the experimental ones. The averaged correlation is shown in a dotted line whereas the optimal line, with a slope of 1 and an R² of 1, is shown in a solid line.

Apart from the pressure distribution, also the model stiffness was evaluated. We did that by comparing the total contact forces resulting from the subject-specifically assigned displacements (Figure 7a), which deviated from the experimental ones by 3-9% up to 700 N and by 10-12% from 800 to 1000 N (Figure 7b). The subject-specific stiffness correlated on average moderately with Lin's CCC of 0.82 (range 0.65-1.00, 4 moderately, 3 excellent) [70].

When evaluating the force share among the two forearm bones, we found that on average, in the experiment 57.2 ± 18.2% of the force were transferred via the radial column, the simulation predicted 51.7 ± 15.7% at 1000 N (Figure 8, Table 1).
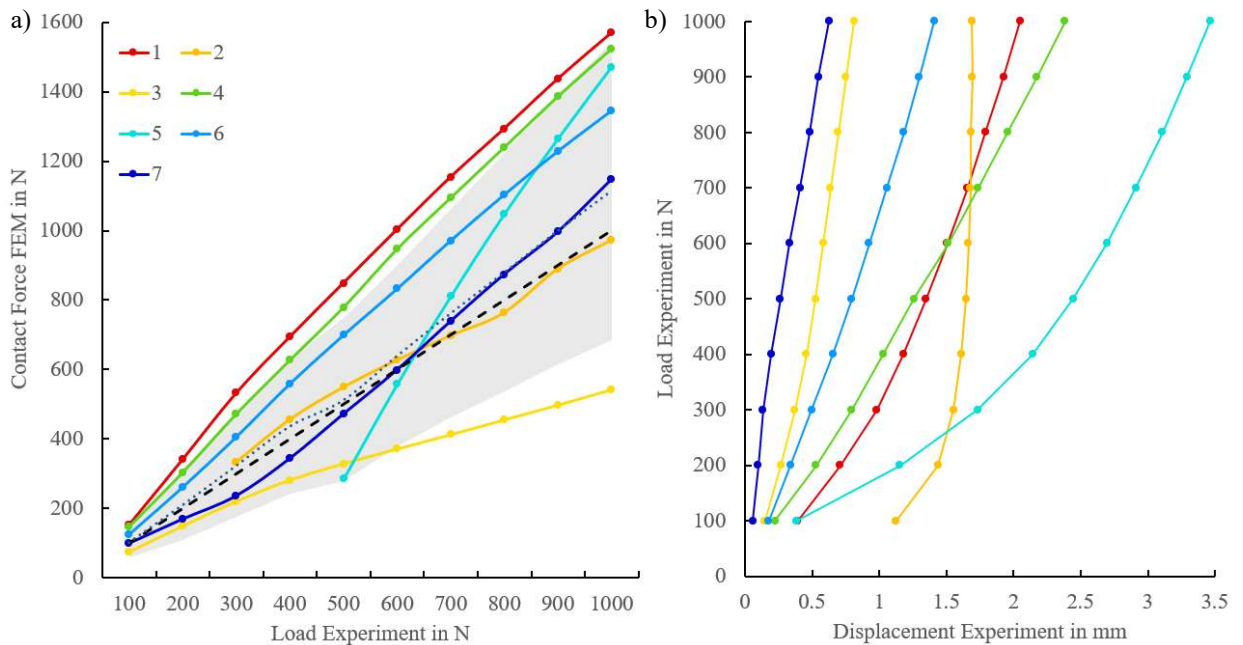
Figure 7: a) The contact forces of the simulation are guided by the displacements measured in the subject-specific experiment. Shown here is the contact force of the simulation over the experimentally applied load subject-specifically for the seven test-specimens, their 95 % confidence interval (grey area), their average (short-dotted line) and the optimal correlation with a slope of 1 (long-dotted line).
b) Experimentally measured loads over displacements of the seven test-specimens. The seven specimens show different stiffness and non-linear behavior, especially for lower loads.

In general, no particular correlation between contralateral specimens was apparent in the experimental parameters or results, therefore any correlation in the simulations would be incidental and was not tested.

2.4 Discussion

In this study, we developed a finite element workflow for the elbow, which includes both the radio-capitellar and the ulno-trochlear joint, that ranges up to realistic loads and that is compared to cadaver tests.
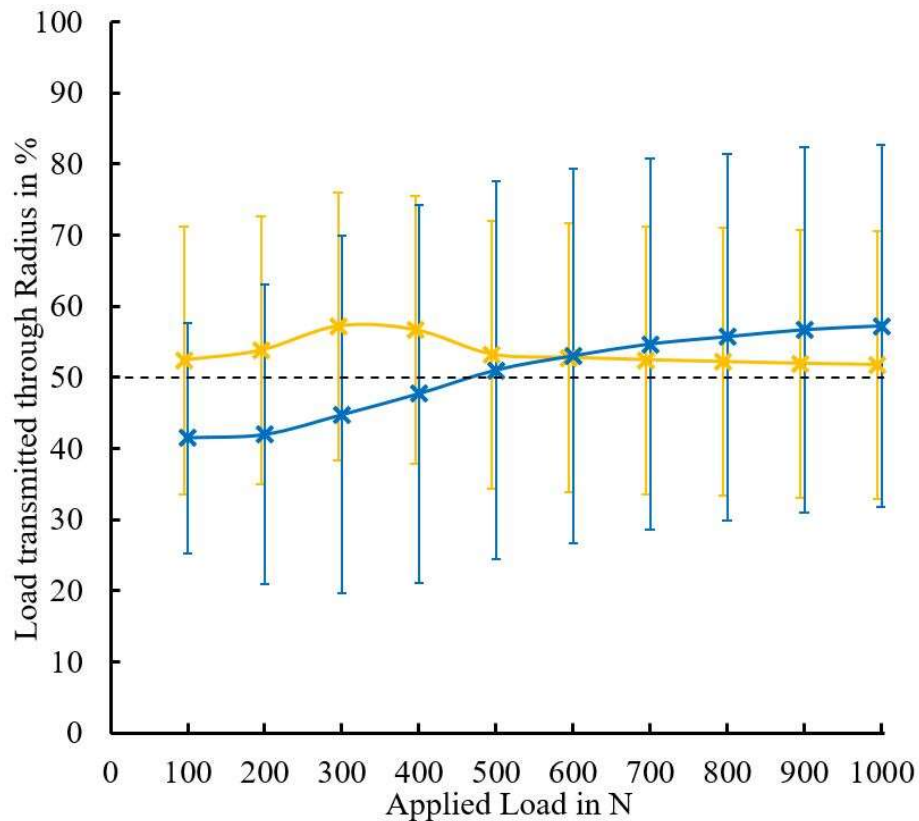
Figure 8: The average share of the total load (mean ± standard deviation) transmitted by the radius is below 50% in the experimental (blue) load cases up to 400 N. The simulated (yellow) share is overpredicted in the loads up to 500 N and underpredicted over 600 N.

The experimental and simulated pressure distributions correlate moderately to strongly in 6 out of 7 cases, in one weakly, the stiffness moderately to excellent [70]. Further, the peak pressures were predicted in the correct joint in all specimens: 6 in the radio-capitellar and one in the ulno-trochlear joint. This outcome was expected when considering the peak pressure an indicator for risk of fracture and radial head fractures being the most common fracture of the elbow [71,72], more common than coronoid fractures. This finding might suggest that the radius possibly fractures first and only with sufficient remaining impact energy, the coronoid fractures second.

Yet, the simulated load share, contact area and peak pressure magnitude only correlated weakly to moderately with the experiments. In our experiments, the radius took up $57.2 \pm 18.2\%$ of the applied 1000 N, in our simulation $51.7 \pm 15.7\%$. These values are similar to the literature: Hackl et al. observed load shares on the radius between $55.0 \pm 15.1\%$ and $66.5 \pm 16.1\%$ of the applied 50 N to 400 N in 14 cadaveric specimens in full pronation [12]. Halls and Travill reported that in a study with 7 cadaveric specimens, on average 57% of the 150 N applied to the hand were transferred over radio-capitular column to the humerus [13].

Further, our average contact area measured at 1000 N was, with 395.4 mm², similar to the strongly varying literature data: Willing et al. reported of 342-375 mm² at 80 N whereas Smithson et al measured around 275 mm² at 100 N [11,14]. Our simulations underestimated the contact area, and peak pressure magnitudes only correlated weakly, which might be due to the manually adjusted constant cartilage thickness up to contact. That is also why our model was not able to predict the missing contact in two cases for lower loads - a discrepancy to the experiments. Since our CT parameters were focused on the bone, the cartilage geometry could not be extracted. Therefore, we assigned a constant cartilage thickness like Kim and Miller [10]. When varying the thickness from 1.1-0.9 mm, the maximum contact stress changed by 7.5%. In our study, the cartilage thickness was adapted to the joint gap after registration of the digital to the experimental bone positions and ranged from 0.7-1.1 mm among the different specimens. We could not detect a correlation or a trend between cartilage thickness and peak pressure. Future studies should overcome that inaccuracy with optimized CT parameters, as studies showed that the cartilage geometry does impact contact mechanics [11,55].

By allowing for self-alignment in the experiment, contact at lower loads will be improved and the poor practice of linearization, based on loads over 400 N, can be avoided. The simulated peak pressure magnitude might differ from the experiments due to the soft tissue missing in the model but being intact in the experiment, as far as inserting the pressure mapping sensor allowed for. Future studies should address this discrepancy by representing all relevant structures. Apart from that, even though the pressure mapping sensor is pre-conditioned and calibrated, diminishing load output over time and with repeated use cannot be excluded [63].

Subjecting the FEM to realistic loads is necessary in order to transfer the results to real-life situations [73], which are reported as 1600 N in the ulno-humeral and 800 N in the humero-radial joint [60]. Balancing the real-life loads and the risk of off-axis fractures starting at 1448 N [74], we decided for a maximum load of 1000 N. When analyzing the 95 % confidence interval of the predicted contact force (Figure 7a), one has to consider the limits of this statistical parameter in non-normal distributions, particularly with small sample sizes [69].

Even though most steps of the Reporting checklist for verification and validation of finite element analysis in orthopedic and trauma biomechanics [75] were followed, the workflow can be improved with a four-eyes principle observing the critical parameters. Apart from that, more outcome parameters could be evaluated, e.g., full-field optical measurements at the cost of soft tissue coverage or strain gauges serving as local validation points. The relevance of the

uncertainty quantification grows with increasing precision and accuracy of the model predictions and is related to the research question the model is designed for.

The published workflow with parameters derived from one specimen can predict the stiffness, pressure distribution and peak pressure location properly for the 7 specimens of the test cohort. It may serve as groundwork for further research, which should focus on improvement of the cartilage contact. We believe that this study presents a solid base for simulations aiding in prosthesis design as well as fracture prediction.

2.5   Contributions

In this study, Stephanie Kahmann was responsible for the conceptualization from the clinical problem to the research question and the overarching research goal. She designed the methodology and created the models (biomechanical and computational). The validation of the models with literature and biomechanical data, the formal analysis of all results using custom-written code for mathematical and statistical descriptions, the investigation in terms of data collection, and the data curation, consisting of filtering and scrubbing raw data, were performed by her. Apart from that, she wrote the original draft of the manuscript, visualized all data and was responsible for the project administration.

Amelie Sas provided scripts to automate some processes in the model preparation and reviewed and edited the manuscript.

Nils Große Hokamp supplied the CT data that met the specific requirements stated by me, and also reviewed and edited the manuscript.

G. Harry van Lenthe supported me in the methodology and formal analysis. He supervises me as Mentor during my PhD and reviewed and edited the manuscript as well.

Lars Peter Müller provided the resources and funding.

Kilian Wegmann also provided the resources and funding, supervises me as PhD advisor and reviewed and edited the manuscript.

2.6   Acknowledgements

Chapter 3

The automized fracture edge detection and generation of three-dimensional fracture probability heat maps

The automized fracture edge detection and generation of three-dimensional fracture probability heat maps

Stephanie L. Kahmann[a]*, Valentin Rausch[a], Jonathan Plümer[a], Lars P. Müller[a], Martin Pieper[b], Kilian Wegmann[a]

[a] Faculty of Medicine and University Hospital, Center for Orthopedic and Trauma Surgery, University of Cologne, Kerpener Str. 62, 50937, Cologne, Germany

[b] University of Applied Sciences Aachen, Heinrich-Mußmann-Str. 1, 52428 Jülich, Germany

*Corresponding author.

Adapted from:

3.1 Introduction

In orthopedic surgery, a new trend is the retrospective statistical analysis of fracture patterns in large patient collectives [49,50,76–91]. These analyses have demonstrated shortcomings in fracture classifications [79,87,90,92] and implications for surgical techniques [49,84,87]. However, a hurdle in creating these evaluations is the extensive manual labor and that they are prone to inter- and intra-observer deviations [90]. These drawbacks could be overcome by an algorithm that can perform parts of this task automatically, thus promoting the statistical analyses of all common bone fractures.

The first studies that have analyzed fracture patterns three-dimensionally, have examined 3D CT scans and transferred the fracture lines to a 2D reference image for the statistical analysis [49,50,78,81,83–87,90]. Later, both the analysis and the mapping have been performed in 3D [76,77,80,82,89,91]. To this point, this technique has been applied to fractures of the tibia [76,77,85–88], the femur [80,91], the patella [83], the proximal ulna [49], the scapula [81,84,89], the distal radius [50,78,79] and the humerus [82,90].

Thus far, these evaluations have been performed manually, without any automation of the process. However, increased automation in this process can provide various advantages. Automated processes guarantee that the same input always produces the same results without the risk of a bias produced by the respective investigator. Furthermore, a higher proportion of automation facilitates the analysis of large amounts of data in a short time without requiring the valuable time of experts. This time saving can also promote subsequent iterated subgroup analyses.

Several steps in the analysis of 3D-images would be suitable for a higher degree of automation. Fürnstahl et al. have automated fracture reduction [93] in order to improve preoperative planning of complex fractures. Their method requires a CT scan of the intact contralateral side for reference. Later, Vlachopoulos et al. have developed a method independent of the contralateral side [94]. They gave up the automatic step of edge detection from Fürnstahl et al. [93] and instead manually placed points on the edges to allow for a curvature-guided reduction of the fracture. Both studies are strictly aimed at computational fracture reduction.

To the best of our knowledge, no algorithm to automize the fracture edge detection and generate a heat map has been developed. We hypothesize that such automation can perform the formerly

manual task faster and with little error. A deviation between the manual and the automized approach in the magnitude of 5.0 mm is considered acceptable [89].

3.2 Fracture analysis method

In the following, the steps of the new algorithm are described in detail. First, the data is prepared in manual pre-processing. The automated algorithm consists of three parts: the transformation of the template, the fragment edge detection, and the generation of the probability heat map. The algorithm is tailored for CT scans with a minimal slice thickness of 2 mm, all CT scans included in this study fulfill this requirement.
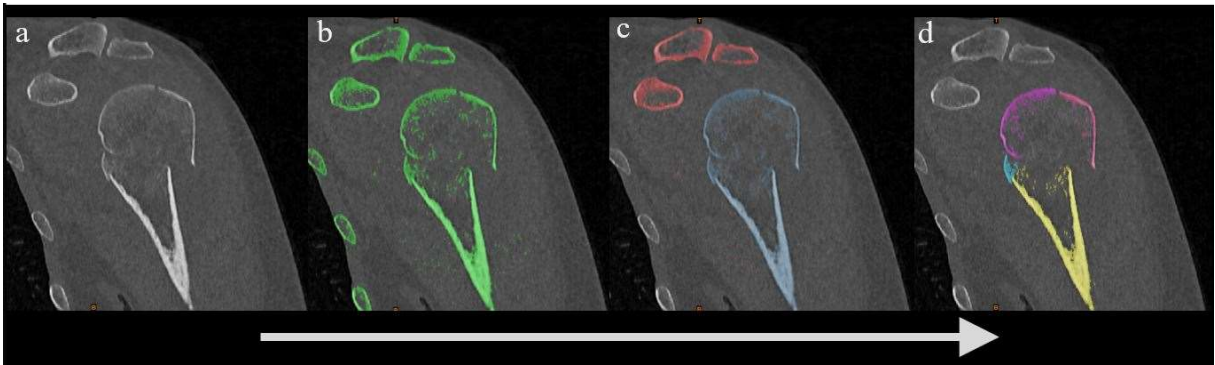
Figure 9: Segmentation workflow. The analysis is based on CT scans of fractured samples (a), in this example a fractured proximal humerus. Each scan is manually segmented (b), the bone is highlighted in green. The bone is split (c) into humerus (blue) and surrounding bone (red). This humerus is then split (d) into four separate fragments, visible in yellow, blue, pink and purple.
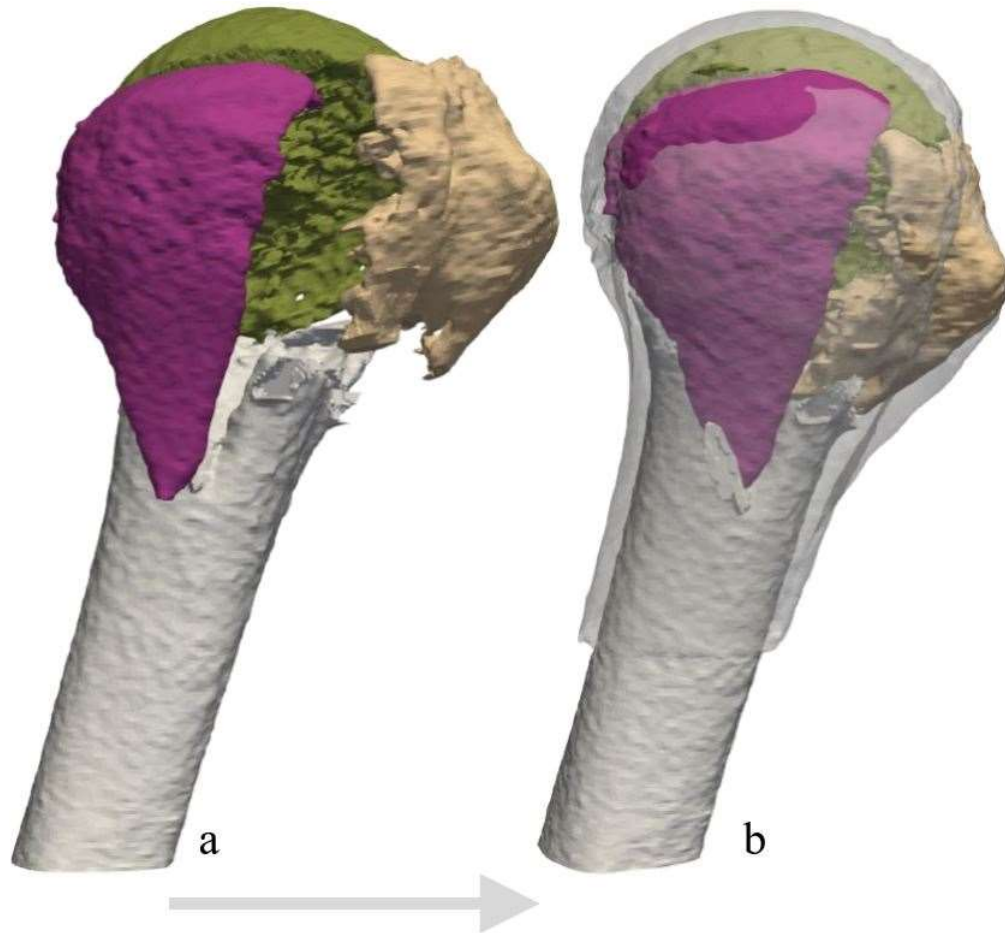
Figure 10: Manual fracture reduction. The displaced fragments (a), shown in green, purple and beige, are manually reduced with the aid of the template (b), shown in semitransparent grey.

Pre-processing: data preparation

In pre-processing, the bone geometries of all fractured specimens and the intact template are extracted: This is performed semi-automatically with a script automatically calling the implemented functions of the segmentation software (Mimics 20.0, Materialise NV, Leuven, Belgium), which are executed interactively by a user. Each CT scan (Figure 9a) is segmented using the default threshold for bone of 226 HU [82] (Figure 9b) and the desired bone is split from the surrounding ones (Figure 9c). In the fractured specimens, the geometry is split into separate fragments (Figure 9d). Analogously to the method from [94], the orthopedic surgeon performing the manual pre-processing distinguishes between large fragments that would be re-fixated in surgery and the small ones that would not. The small fragments remain attached to a neighboring fragment. The template is segmented in the same way, omitting the fragment splitting. In the proximal humerus analyses, the template geometry is based on an intact right humerus CT, that is independent of the fractured specimen. To obtain only ipsilateral samples, the samples of left humeri are mirrored along the sagittal plane, leading to only right humeri.

In the analyses of the distal humerus, the tibia plateau, the scaphoid and the acetabulum fracture, templates of the same side are used. With the aid of the intact template, the displaced fragments (Figure 10a) are manually reduced (Figure 10b). The orthopedic surgeon translates and rotates each fragment separately to its pre-fracture position using common transformation functions, approximating the shape of the intact template as a reference. In the last manual pre-processing step, the template and all surface geometries of the fragments are exported to serve as input for the fracture analysis tool. This manual pre-processing had been performed for a former, yet unpublished study already. Optionally, the template resolution can be down sampled to accelerate the transformation process, although this comes at a cost to accuracy.

The fracture analysis tool

The fracture analysis tool is implemented in MATLAB (MathWorks, Natick, Massachusetts, USA) Version 2018b. It requires the surface geometries of the template and the fractured samples as a stereolithography file input. The tool runs all processes automatically over a defined batch and returns a heat map of all included fracture edges as an output.

Template transformation

In the template transformation, the surface geometries of the fractured humerus and the intact template are imported and processed. The intact template is successively transformed onto the different samples (Figure 11a). From the two options to transform either the lower resolved intact template or the higher resolved fractured specimens, we decided for the intact template. This way, the intact template maintains a homogeneous distribution of the points, reacts more robust to holes from bony defects and the process is faster than deforming the fractured samples. In detail, the template point cloud is scaled to 110% of its original size and then shrunk non-rigidly to the smaller sample data from the outside in. This ensures that the transformation of the target represents the outer surface of the sample. Thus, it is not diverted by the inner surface of the cortical fragments or by the spongious bone within the humerus. This facilitates the manual segmentation as it is no longer necessary to remove the inner surface as in other methods [93] or to distinguish between cortical and spongious bone. Additionally, including spongious bone reduces the risk of neglecting low density cortical bone.

The transformation is performed with a non-rigid iterative closest point algorithm, based on the one published by Amberg et al. 2017 [95]. First, the manually pre-aligned template is registered to the fractured sample with a regular iterative closest point algorithm. Then, in the non-rigid

algorithm, a cost function is minimized, consisting of two terms. The first term describes the distance between the template point cloud and the sample point cloud. The second term describes the stiffness of the transformation matrix. It regularizes the deformation of the template by penalizing large differences in the transformation of neighboring points. This causes of neighboring points to transform similarly, thus results in a smooth global mesh. To avoid the overdetermined system of linear equations with matrices close to singular, we replaced the solution algorithm of the optimization problem. The original algorithm uses ill-conditioned normal equations $A^T A x = A^T b$, where A^T is the transpose of system matrix A, x is the minimal solution vector and b is the right-hand side vector. Instead, we apply the method of least squares by a QR decomposition. This approach decomposes the system matrix A into the two factors Q, an orthogonal matrix, and R, a right triangular matrix. It finds the minimal solution vector x with respect to the Euclidean norm $||\cdot||_2$ for the right-hand side vector b. The solution vector x describes the transformation of the undeformed vertices onto the target. For a detailed description, we refer to [95]. Golub et al. have compared both approaches and found that the QR approach for solving least squares minimizations of the form $||Ax\text{-}b||_2$ with respect to the Euclidean norm "is more appealing in situations where b is close to the span of A's columns" [96]. Thus, the QR approach provides a robust solution that also allows computations with matrices with high rank deficit, as is the case in this application.

Edge Detection

Edge detection is conducted using the transformed template with a loop over all fragments of each sample consecutively. In the first step, the points in the transformed template corresponding to the first fragment, the first fragment point set, are found with a range search function (Figure 11b). In the second step, these points are transferred to the undeformed template via point ID (Figure 11c). There, to each point of the first fragment point set, the neighbors in a defined vicinity are found. If the point only has neighbors that are part of the first fragment point set, it is ignored. If it has neighbors that are not part of the first fragment point set, it is declared an edge point (Figure 12a). This way, all points that have neighbors from a foreign fragment are considered edge points. The radius of the vicinity depends on the resolution of the template point cloud. The previously processed fragment points are excluded from the remaining point cloud. Ultimately, all fragments are processed this way (Figure 12b). The points considered an edge point are marked and can be processed in the heat map generation (Figure 12c).
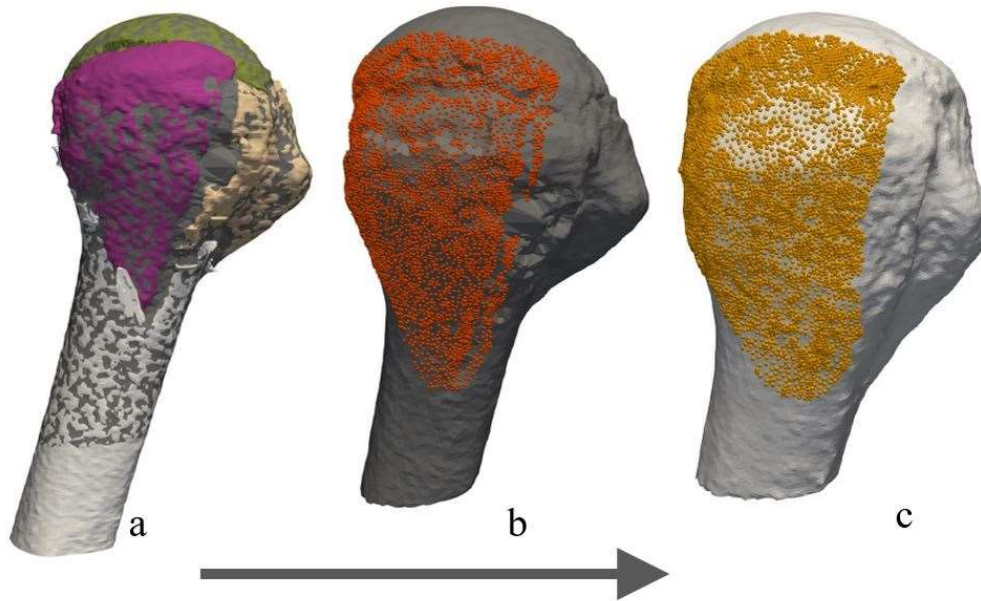
Figure 11: Automatic fragment identification. The template (dark grey) is automatically transformed onto the fractured sample (a). The first fragment (purple) is identified (b) on the transformed template (dark orange). The identified fragment is then transferred to the undeformed template (c) via point ID and highlighted in bright orange.

Heat map generation

The heat map is generated by using the detected edges to evaluate the regional probability of fracture. The detected edges of all samples are superimposed and represented by a color-code projected on the surface of the original shaped template (Figure 12d). The color-code indicates the frequency of fracture edges superimposed in each node. This fracture probability heat map reveals information about the prevalence of common fracture sites.
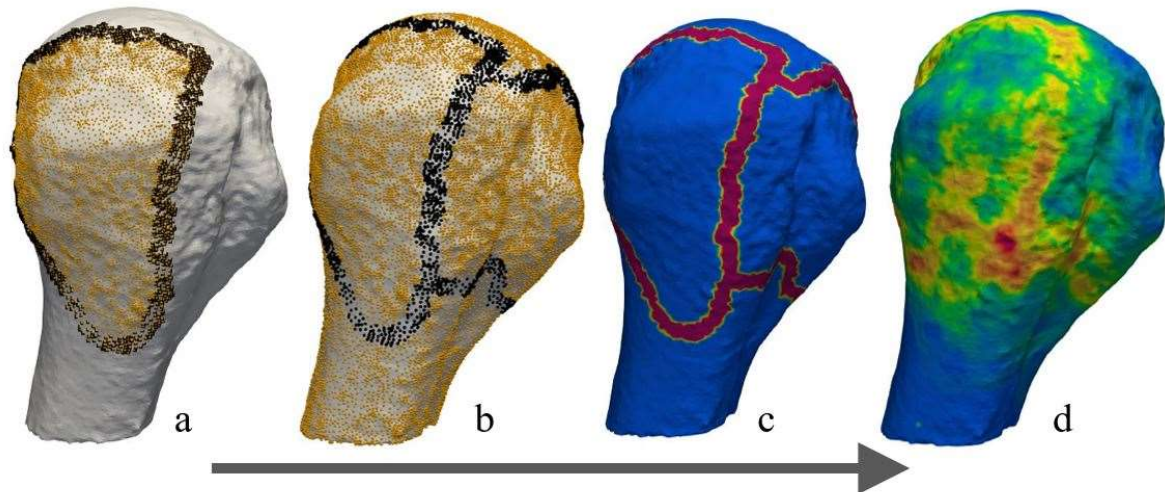
Figure 12: Automatic edge detection and heat map generation. The detected edge of the first fragment is presented in black dots in (a), the subsequent fragment edges are found in the same way, iterating over all fragments (b). The heat map with only one sample is shown exemplary in (c), and the heat map of 50 superimposed fractures in (d).

3.3 Proof-of-principle analysis

Edge detection in 10 proximal humerus fractures

We evaluate the accuracy of our edge detection tool relative to the current standard method in ten explicitly chosen fractures [89]. The ten fractures are a subgroup, selected to reflect the shape of the histogram that represents the number of fragments in all 50 humeri included in this study, see section 3.3. This way, the most common fracture types are represented, and the relative weighting factor is respected. The ten fractures comprise 2 2-part fractures, 4 3-part fractures and 4 4-part fractures; 60 % affect the greater tuberosity, 60 % the minor tuberosity, 70 % the surgical neck and 30 % the anatomical neck, according to the Codman classification [97]. The mean age of the subgroup is 65 years (range 42-99) (Table 2). The standard method has been to transfer the fracture edges manually from the fractured sample to the intact template. One experienced surgeon performs this manual task while, at the same time, the algorithm detects the edges (Figure 13). Both competing candidates start after the template is transformed. The Euclidean distance from all edge points between both outcomes is evaluated, as well as the time cost. We run all analyses on a machine with an i7 CPU (2.2 GHz) and 16 GB RAM, in the 64-Bit operating system.

The averaged Euclidean distance from the manually to the automatically found fracture edges for all 10 humeri is 2.5 mm ± 2.4 mm (mean ± standard deviation). Furthermore, 20 % of all edge nodes match exactly. The manual assignment of the fracture curves took 92 minutes. The automatic edge detection took 23 seconds. The transformation of the template on the ten humeri before the competition took 4 minutes. Consequently, the automatic process is 240 times faster excluding the transformation and 23 times faster including it.

Edge detection in other sites

To test how broadly this algorithm could be applied, we perform the edge detection on distal humerus, tibia plateau, scaphoid, and acetabulum fractures. The numbers of triangles of each sample and its respective template as well as the run times and cohort information can be found in Table 2.
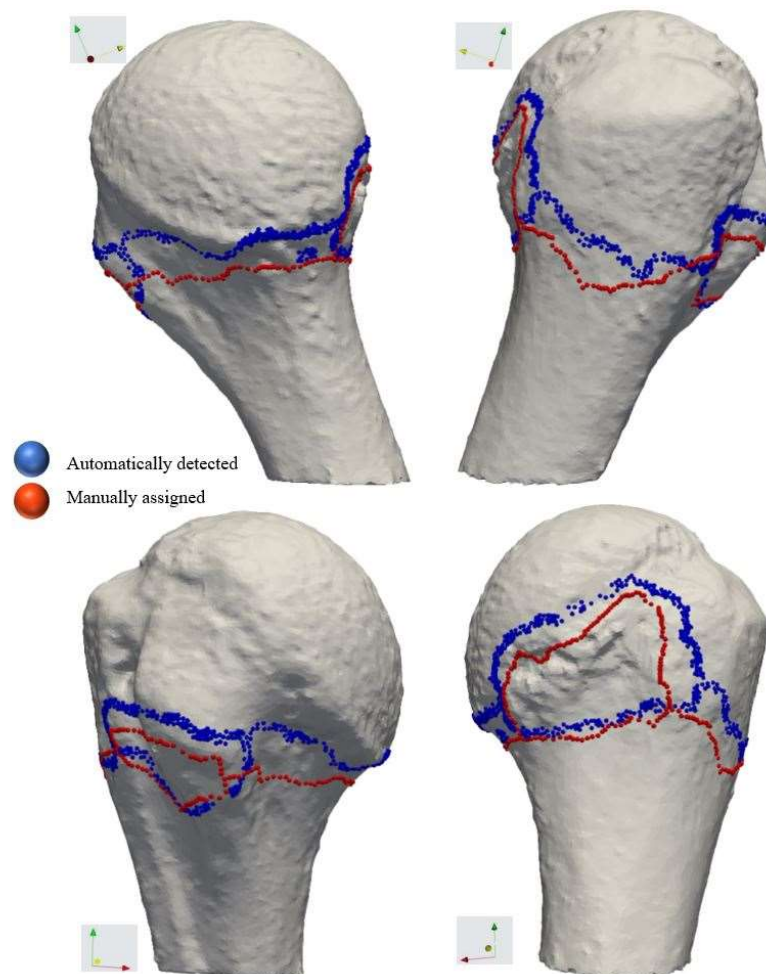
Figure 13: Automatically detected vs. manually assigned edges. On one exemplary fractured sample, the automatically detected edges (blue) and the manually assigned edges (red) can be compared from medial (top left), lateral (top right), anterior (bottom left) and posterior (bottom right) view.

Table 2: Information about the patient cohort included in this study.

Site	Number of triangles	Computation time	Number of fragments	Age in years	Sex
10 proximal humeri fractures	364,453 ± 196,138*	23 minutes	4 ± 1*	65 ± 16*	5 F 5 M
50 proximal humeri fractures	281,663 ± 135,250*	6,5 hours	4 ± 1*	64 ± 16*	28 F 22 M
Tibia plateau	386,776	2 minutes		51	M
Distal humerus fracture	103,066	1 minute	5	79	F
Scaphoid fracture	8,194	1 minute	2	50	M
Acetabulum fracture	1,487,034	78 minutes	6	66	M
Proximal humerus template	44,048			67	M
Tibia plateau template	62,556			43	M
Distal humerus template	18,756			27	M
Scaphoid template	44,024			48	M
Acetabulum template	1,488,536			64	M

*mean ± standard deviation

The automatic edge detection finished quickly (≤ 2 minutes) in the distal humerus, tibia plateau and scaphoid fractures.

The acetabulum has the most complex shape of all examples. To account for that, the number of triangles in the fractured sample (1,487,034) and the template (1,488,536) are substantially higher than in the other sites. As a result, the runtime of the transformation of the acetabulum is by far higher (78 minutes).

The automatically detected edges are found correctly for the distal humerus fracture (Figure 14a), the tibia plateau (Figure 14b) and the scaphoid (Figure 14c) according to visual judgement by the orthopedic surgeon. In the acetabulum (Figure 14d), a few outliers were considered edge points, possibly due to poor bone quality in the fractured sample.
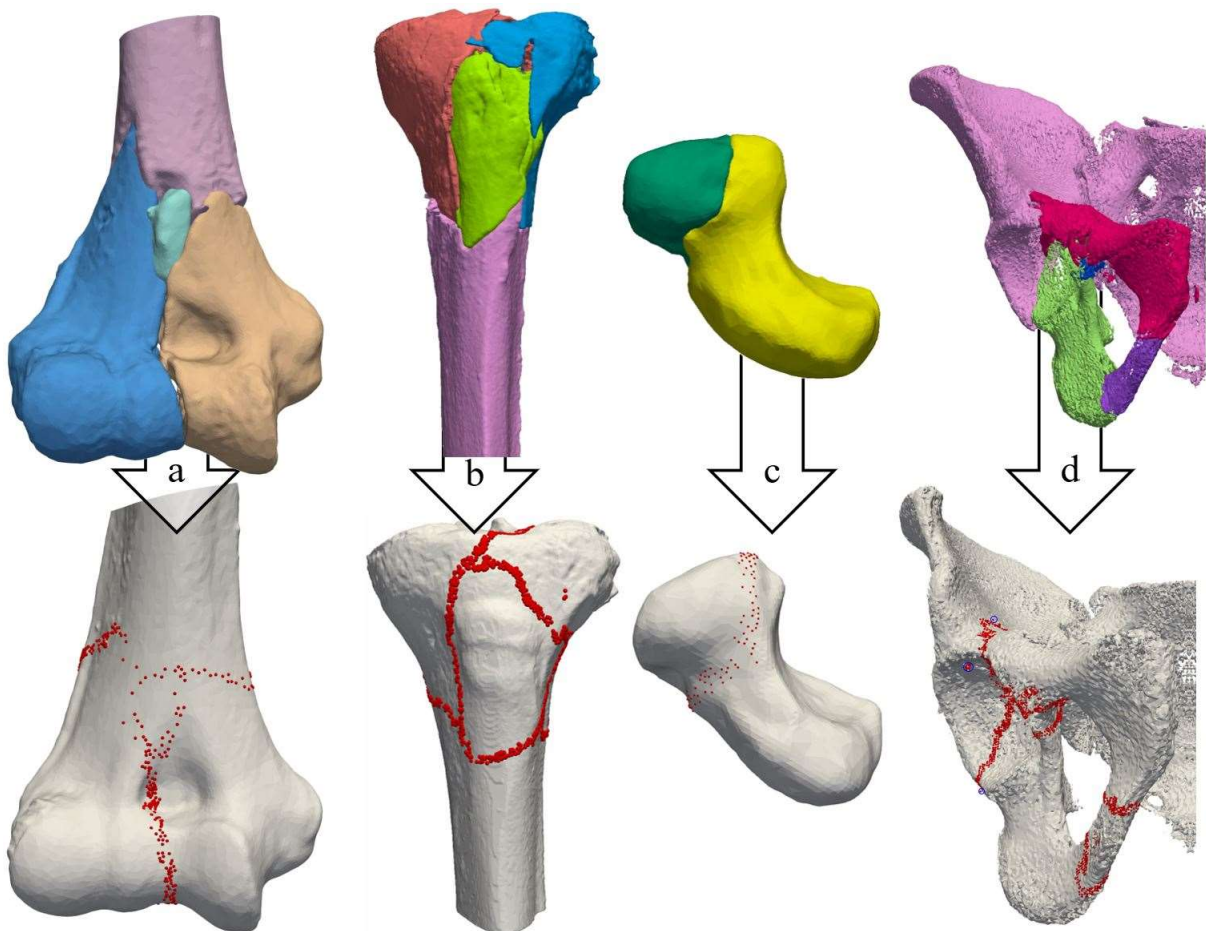
Figure 14: Automatically detected edges in different sites. The top row shows a distal humerus fracture with 5 fragments (a), a tibia plateau fracture with 5 fragments (b), a scaphoid fracture with 2 fragments (c) and an acetabulum fracture with 5 fragments after the last manual step, the fracture reduction. The bottom row shows the corresponding automatically detected fracture edges. In the acetabulum, outliers in the detected edges are highlighted with blue circles.

Heat map approach with 50 proximal humerus fractures

We present a heat map generated with 50 proximal humerus fractures to demonstrate the possible clinical applications of our statistical evaluation (Figure 15). This cohort comprises 50 patients that presented consecutively at University Hospital Cologne in 2016, received CT scans of the proximal humerus, were over 18 years old and had no arthrosis. Their mean age is 64 years (range 24-99 years). The Codman classification [97] showed that 82 % of the fractures affect the greater tuberosity, 32 % the lesser tuberosity, 74 % the surgical neck, and 14 % the

anatomical neck; the 50 fractures comprise 15 2-part fractures, 21 3-part fractures, 12 4-part fractures and 2 5-part fractures. The heat map is generated by superimposing the automatically detected fracture edges of all 50 samples. The generated heat map shows the frequency with which a fracture occurred in each node, which can provide information about fracture probabilities in specific locations. Here, we find a high probability for fractures which are in line with those described in the medical literature [98]. Main fracture lines project on the greater tuberosity and on the anatomical neck of the humeral head, which are among the most common injuries to the proximal humerus. We also find that the articular surface was rarely involved, which corresponds with the rarity of reported injuries that involve the articular surface in the medical literature [90] and in clinical practice.

Figure 15: Heat Map of 50 proximal humerus fractures. The superimposed fracture lines of 50 fractured humeri are color-coded to form the heat map. The color bar indicates the frequency of fracture occurrence in each point.
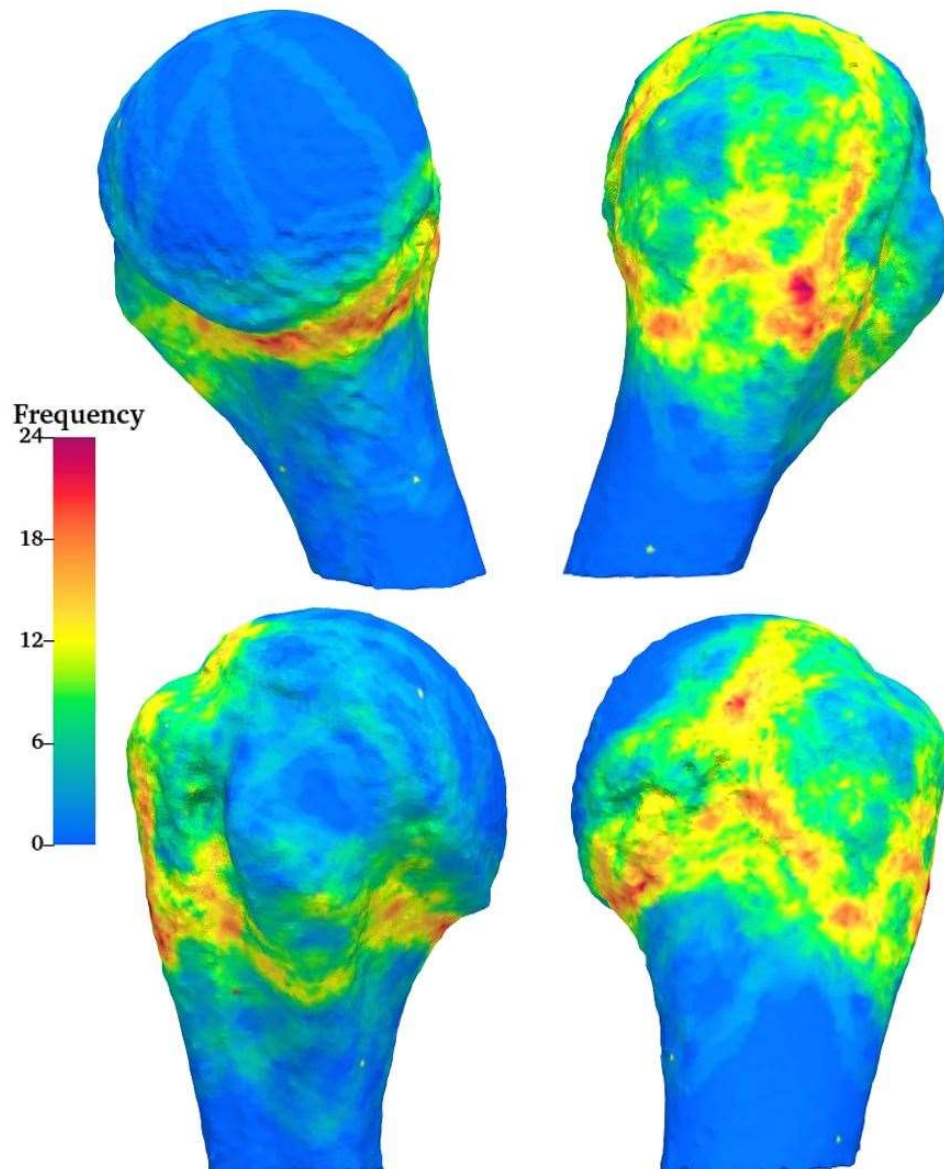
3.4   Discussion

We present an algorithm that can detect fracture edges in a reliable, accurate, and quick manner. It is applicable to a broad variety of fractures as it can detect edges in different shapes. The generated heat map reveals valuable information about common fracture patterns and regions with a high risk of fracture.

Our algorithm runs 23 times faster than the manual assignment in our study of 10 proximal humerus fractures. The manual assignment corresponds to the method applied in [76,77,80,82,91]. Both approaches have in common the manual pre-processing, which includes the segmentation of the CT Data, the splitting of the fracture and the fracture reduction. However, in the manual gold standard, also the fracture edge detection and their superposition are performed manually, whereas these steps are automized in our algorithm. In some studies, the fracture edges have only been superimposed to give information about the fracture distribution. In other studies, image processing software was applied to produce color coded heat maps. In our algorithm, the heat map generation is already integrated but could be converted into a simple one-colored fracture edge distribution. Similarly, Fürnstahl et al. demonstrated, that the fracture reduction can be automized in a study with six proximal humerus fractures [93]. Based on manually segmented and split CT data from a former study, their algorithm rigidly transforms the fragments to the correct position with the aid of the contralateral side. However, since the fracture reduction had been performed for a former, yet unpublished study already in our case, there was no necessity to automize this step for us.

One drawback of our automated process is the high run time for complex geometries with many nodes, as seen in the acetabulum with 78 minutes. The increased computational time does not, however, require continuous human input but can run on the machine without interaction. Furthermore, the appropriate trade-off between accuracy and speed can be found by down-sampling of the original data: in the case of the complex shaped acetabulum, we considered the few outlying points acceptable at the run time of 78 minutes. With higher resolution and higher computational power, even the evaluation of complex shapes becomes feasible. In addition, the runtime of 78 minutes was a strong outlier compared to the runtime of maximally 2 minutes for the proximal humerus, the distal humerus, the tibia plateau, and the scaphoid fractures. Since in 4 out of 5 sites, the automatic edge detection ran within (less than) 2 minutes per sample and the manual assignment took almost 10 minutes per sample, we conclude that the hypothesis, the algorithm runs faster, is fulfilled for simple geometries.

The other drawback is the slight deviation from the manually assigned fracture lines of 2.5 mm ± 2.4 mm. This deviation can be impacted by the resolution of the template. When considering this deviation, it is important to note that manual evaluation is subject to individual deviations, which is reflected in reported measures of inter- and intra-observer reliability [90]. In contrast, the automatic process always delivers the same output for the same input. Dugarte et al. compared the more sophisticated 3-dimensional fracture edge assignment to the 2-dimensional gold standard. In a study with 10 scapulae, they found mean deviations of 5.7 mm on average (range 4.0 to 10.4 mm mean deviation within each subject) [89]. We also evaluated the new compared to the former approach by comparing 10 samples. Since in other studies with manual edge detection no inter- or intra-rater deviations had been reported, we applied the result from Dugarte et al. as a threshold for our hypothesis. We stated that a deviation of (down rounded) 5 mm between the manual and the automatic edge detection was acceptable. With a deviation of 2.5 ± 2.4 mm, this hypothesis is fulfilled.

Purposely choosing 10 proximal humerus fractures reflecting the histogram of the 50 humerus fractures could be criticized since they are not randomly chosen. However, this way the algorithm was tested for differently complex fractures. Furthermore, this choice is based on the number of fragments rather than a classification to reduce subjective input. However, to report on the severity of all included fractures, we applied the relatively reliable classification by Codman [97,99].

The number of 50 samples included in this study is in the lower range compared to some other fracture pattern analyses (38 samples in [85] to 353 in [77]). This might lead to limited representation in the heat map. However, the focus of this study lays on the feasibility of the method and not on the clinical implications.

Regarding the clinical implications, fracture probability heat maps reveal valuable information about fracture patterns as demonstrated by Kfuri and Schatzker, who adapted their tibia plateau classification based on fracture mapping [92].

Automizing this proven concept comes with a risk. The non-rigid iterative closest point algorithm harbors the risk of causing a distorted mesh. However, Amberg et el. demonstrated the regularity of their transformation with a complex example. In the test, the template was transformed onto an incomplete, rigidly transformed, and non-rigidly distorted cube. They declare the algorithm performs "accurately" and the mesh remains smooth since a projected

checkerboard pattern was still uniform and an inscription readable after transformation [95]. This capacity is not affected by our substitution of the solution algorithm.

We conclude that our hypotheses are fulfilled for simple geometries, where it can reduce the time consumption by a factor of 20 and with a deviation of 2.5 mm ± 2.4 mm. Once the transformation is performed, the algorithm offers the option to divide the cohort into sub-groups by assigned properties and to re-calculate the heat map in a very short time. This would allow for several options such as the validation of regularly used classification systems or a subgroup-analysis of patients grouped by sex, age, or injury mechanism, which could only be achieved with a much greater effort when performed manually. Future work should aim towards full automation of the process, including the segmentation, fragment identification and fracture reduction.

3.5 Contribution

In this project, Stephanie Kahmann was responsible for the conceptualization of the research question, the development of the methodology, the design and generation of the algorithm, validation of the algorithm, formal analysis of the generated data as well as curation of the raw data. She wrote the original draft, including the visualization of all data and took on the supervision of the research project and the project administration.

Valentin Rausch supported me in the conceptualization and assisted in the investigation. He supported the resources and reviewed and edited the manuscript.

Jonathan Plümer assisted in the investigation.

Lars Peter Müller aided in the resource and funding acquisition.

Martin Pieper supported in adjusting the optimization algorithm in the software.

Kilian Wegmann provided the resources and funding for the project.

Chapter 4

General Discussion

General Discussion

The terrible triad injury of the elbow remains a challenging injury with varying outcome and no consensus on one optimal surgery protocol can be derived from literature. To improve the situation for patients, more data on the TTI is required. We aimed to gather more data from an FEM of the elbow, as described in **chapter 2** [5]. Since before, no published finite element model provided all relevant data, the input parameters were sampled from different models. To ensure their valid interaction even though stemming from different sources, we carried out several parameter studies as well as effect size studies, which poses a relevant step towards validation. With the publication of this finite element workflow, the first model representing all relevant bones and joint contacts has been made available.

With the presented finite element workflow, the groundwork is laid towards a validated finite element model of the fracture mechanism. The finite element workflow could predict the experimental contact pressure with moderate to strong correlation in 6 out of 7 cases, the stiffness with moderate to excellent correlation and the peak pressure in the correct joint in all 7 cases. This means that the aim, to design a model that can predict these two parameters with on average moderate correlation and in the correct joint, has been fulfilled. One strength of the study lies in the close combination of experiment and simulation, rooted in the subject-specific CT data and the registration by means of tantalum beads. This allows for a close calibration of the model parameters in the one model used of optimization and a critical evaluation of their impact in the test cohort of 7 specimens. However, the predictions of peak pressure magnitude, contact area and load share with poor to moderate correlation demonstrate the limitations of the model. In these regards, it can still be improved in order to approach the state of a validated model.

Firstly, in the finite element model the representation of the cartilage can be improved. Its geometry could be derived more precisely from CT data with different CT settings. The scanning properties in our study were optimized for segmenting the bone, based on data provided by Dahan et al. for their study of the proximal humerus [100]. However, as demonstrated by Willing et al., the cartilage thickness varies locally and influences the contact mechanics. Furthermore, the cartilage material properties need to be reflected correctly. However, the material model described by Willing et al. could not be implemented in the model of our study since it was designed to reflect on a load case of up to 80 N only [11], whereas our model is subjected to up to 1000 N. To enable convergence, we simplified the material

properties to a linear elastic model, even though a minor, non-significant effect of this on the maximum contact stress was described by Kim et al. [10]. Therefore, we assume that refinement of the cartilage shape and material properties will improve the correlation of our finite element model with the experiment. In future research, it has to be investigated if the Mooney-Rivlin material model, as recommended by Brown at al., also proves correct for the strain rates of a high-impact fracture [101].

Secondly, it was mentioned that no stabilizing soft tissue was included in the model. Based on the clinical studies observing stability after different reconstruction protocols, it can be derived that the physiological model should cover the MCL, the LCL complex and the anterior capsule [28,32,40]. If the muscles need to be included in the finite element model, possibly in terms of nodal forces [102], needs to be investigated in a separate parameter study. Once the physiological model is validated, the influence of the ligaments on the fracture pattern and then the possible influence of the joint displacement on the ligaments can be investigated.

In the experiment, improvement can be achieved by allowing self-alignment of the joint. In the presented set-up, the bones were fixed rigidly in resin both at the humeral site and the radial and ulnar site. The reason for that was to ensure a stable and well-controlled position of the bones during all load steps. However, this kept the joint from aligning physiologically. In a future study, the balance between a stable and controlled position and a dynamic alignment needs to be found. The risks are either a too rigid fixation, that prevents the joint from aligning or an insecure fixation that could allow for bending and therefore promote premature fractures in the shafts of the long bones or a loosening during the load steps and therefore motion that cannot be predicted correctly in the finite element model.

In the next step, digital image correlation (DIC), a non-contact optical measurement method, can be applied. Non-contact measurements have the advantage of very low interference with the mechanical properties of the specimens. DIC allows for a comparison of the strain distribution on the bone surface between the simulation and the experiment. This poses a crucial step towards the correct fracture prediction of the TTI since strain is commonly regarded an indicator for bone fracture [103,104] and its correct prediction dependent on experimental validation [8]. However, optical strain measurement comes at the cost of required direct visual access: the specimens need to be stripped off all soft tissue.

Starting with our study, different adaptations can be implemented to address specific research questions. From the physiological model in pronation and full extension, models in other

positions can be derived to predict the mechanical response in other critical or common situations. Apart from that, joint replacement implants can be tested in this model. Thus, their design can be improved to match the physiological joint contact mechanics. By this means as well, the perspective regarding the outcome could be improved for patients with terrible triad injuries.

The algorithm presented in **chapter 3** facilitates the evaluation of fracture patterns from CT scans as the manual input is reduced strongly [6]. All hypotheses were fulfilled as it runs 23 times faster and with 2.5 ± 2.4 mm, the deviation lies below the acceptable 5.0 mm, compared to the manual approach. The algorithm excludes both inter- and intra-rater differences since the same input always leads to the same output. Furthermore, it was proven that the approach can be applied to different sites, independent of the general shape of the bone and independent of the severity of the fracture.

The difference between the manual and the automated edge detection can on the one hand be considered the acceptable error for the advantage of the shorter evaluation time and the little manual input. On the other hand, one has to bear in mind that the manual evaluation might also be erroneous, therefore it could be considered only a comparison of two different approaches, not of the algorithm to the correct solution. The found deviation of 2.5 ± 2.4 mm must therefore not strictly be an error but could merely be the difference between two methods.

In the future, the algorithm could be applied to even more sites to explore its limits in diversity of application. Even though a wide range of general shapes has already been tested in the publication, it could be expanded to fractures of the head or face and of other small bones in the hand or foot. As it already proved valuable in long bones with different shaped epiphyses, like the tibia plateau and the humeral head, the algorithm can directly evaluate fractures of the radius and ulna and, therefore, terrible triad fractures. A preliminary study could show if the two bones could even be processed at the same time.

The simplified evaluation would not only allow for specialized care centers to include a larger cohort with the same effort as a small cohort with manual evaluation and therefore show trends even stronger. It would also allow for smaller institutions to assess the fracture patterns as little effort is necessary. This would mean that in addition to the severe fracture patterns, commonly referred to specialized care centers, the milder cases would be represented in the published data. More data allows for a more reliable evaluation of the common fracture pattern and may lead to a more detailed fracture classification. An example for this is presented by Schatzker and

Kfuri who, after statistical evaluations of fracture patterns, revised their initial classification to better represent the different groups [92]. A more suitable classification may be one step toward optimized treatment protocols.

Regarding the method, the conclusive next advancement would be to extend the automation to include even more steps of the currently still manual pre-processing. Fürnstahl et al. demonstrated that the reduction can be automated. Combining these two algorithms will reduce the required manual input even further [93]. Even though they only demonstrated the application of their algorithm to complex humerus fractures, the possibility to expand it to other sites and general shapes of bones should be explored. They also faced the possible problem of the algorithm to cover the irrelevant inner surface of the fragment shells instead of the relevant out surface. In their algorithm, the inner surface of the fracture shells is removed by the algorithm to ensure that the outer surface of the fragments is best matched to the outer surface of the template. The same goal is achieved in our algorithm by only considering the outer surface of the intact template and scaling it to 110 %, then iteratively matching the nodes from the outside in. Combining both algorithms would mean that the scaling of our approach could be neglected.

Compared to Fürnstahl et al., an even more sophisticated approach was presented by Vlachopoulos et al., in which the reduction is independent of the contralateral humerus [94]. This approach is favorable in terms of radiation protection as well as required data of the patient. Overcoming this requirement means that more patients can be included in the study since only the fractured side needs to be CT scanned and not the intact contralateral side. Furthermore, Vlachopoulos et al. also identify the fracture lines, therefore a possible combination with our algorithm can be seen in the post-processing of the reduced fracture lines, particularly since the reduction worked more reliably than in the algorithm by Fürnstahl et al.

Even though artificial intelligence (AI) and deep learning (DL) play an increasing role in image processing in medicine [105], to the best of my knowledge no algorithm identifying fracture edges in 3D using AI or DL has been published. However, classifying fractures automatically using AI has been implemented [106]. This can be helpful for terrible triad fractures in the long term as improved fracture classification contributes to better addressing fractures and outcome: the improvements can come in terms of improved class definitions, better representing the common fracture types as well as in terms of excluded human error like inter-and intra-rater deviations. Further, the role of AI in shoulder surgery is increasing [107] and it is probable that

the application will be extended to the elbow. Common applications are the detection and classification of fractures, where AI outperforms surgeons, as a recently published study shows [108]. Even though AI has been implemented in a broad variety of applications, orthopedic surgery has not benefited greatly of it yet [107].

We conclude that with our work, the next steps in the research on the terrible triad injury are enabled. Even though both publications address basic research, they serve as relevant groundwork strongly facilitating the generation of clinically relevant data. A deeper understanding of the fracture mechanism allows for reliable predictions of affected structures and their suitable treatment. The automation of retrospective fracture analysis and heat map generation will facilitate the gathering of information regarding common fracture lines in the terrible triad injury. Therefore, the incorporated basic research signifies a small but crucial step towards a better prospect for patients with terrible triad injuries of the elbow.

Literature

[1] Hotchkiss, R.N. (1996) Fractures and dislocations of the elbow. In: Rockwood CA, Green DPJ, Bucholz RW, and Heckman J. D., editors. *Rockwood and Green's Fractures in Adults*, 4th editio. Lippincott-Raven, Philadelphia. p. 929–1024.

[2] McKee, M.D., Schemitsch, E.H., Sala, M.J. and O'Driscoll, S.W. (2003) The pathoanatomy of lateral ligamentous disruption in complex elbow instability. *Journal of Shoulder and Elbow Surgery*, **12**, 391–6. https://doi.org/10.1016/S1058-2746(03)00027-2

[3] Stambulic, T., Desai, V., Bicknell, R. and Daneshvar, P. (2022) Terrible triad injuries are no longer terrible! Functional outcomes of terrible triad injuries: a scoping review. *JSES Reviews, Reports, and Techniques*, **2**, 214–8. https://doi.org/10.1016/j.xrrt.2022.01.002

[4] Chen, H.W., Liu, G.D. and Wu, L.J. (2014) Complications of treating terrible triad injury of the elbow: A systematic review. *PLoS ONE*, **9**, 1–7. https://doi.org/10.1371/journal.pone.0097476

[5] Kahmann, S.L., Sas, A., Große Hokamp, N., van Lenthe, G.H., Müller, L.-P. and Wegmann, K. (2023) A combined experimental and finite element analysis of the human elbow under loads of daily living. *Journal of Biomechanics*, **158**, 111766. https://doi.org/10.1016/j.jbiomech.2023.111766

[6] Kahmann, S.L., Rausch, V., Plümer, J., Müller, L.P., Pieper, M. and Wegmann, K. (2022) The automized fracture edge detection and generation of three-dimensional fracture probability heat maps. *Medical Engineering & Physics*, **110**, 103913. https://doi.org/10.1016/j.medengphy.2022.103913

[7] Bryce, C.D. and Armstrong, A.D. (2008) Anatomy and Biomechanics of the Elbow. *Orthopedic Clinics of North America*, **39**, 141–54. https://doi.org/10.1016/j.ocl.2007.12.001

[8] Henninger, H., Reese, S., Anderson, A. and Weiss, J. (2010) Validation of Computational Models in Biomechanics. *Proceedings of the Institution of Mechanical*

Engineers Part H, Journal of Engineering in Medicine, **224**, 801–12. https://doi.org/https://doi.org/10.1243/09544119JEIM649

[9]   Viceconti, M., Olsen, S., Nolte, L.P. and Burton, K. (2005) Extracting clinically relevant data from finite element simulations. *Clinical Biomechanics*, **20**, 451–4. https://doi.org/10.1016/j.clinbiomech.2005.01.010

[10] Kim, S. and Miller, M.C. (2016) Validation of a finite element humeroradial joint model of contact pressure using fuji pressure sensitive film. *Journal of Biomechanical Engineering*, **138**, 2016–9. https://doi.org/10.1115/1.4031976

[11] Willing, R.T., Lalone, E.A., Shannon, H., Johnson, J.A. and King, G.J.W. (2013) Validation of a finite element model of the human elbow for determining cartilage contact mechanics. *Journal of Biomechanics*, Elsevier. **46**, 1767–71. https://doi.org/10.1016/j.jbiomech.2013.04.001

[12] Hackl, M., Wegmann, K., Kahmann, S.L., Heinze, N., Staat, M., Neiss, W.F. et al. (2017) Radial shortening osteotomy reduces radiocapitellar contact pressures while preserving valgus stability of the elbow. *Knee Surgery, Sports Traumatology, Arthroscopy*, **25**. https://doi.org/10.1007/s00167-017-4468-z

[13] Halls, A.A. and Travill, A. (1964) Transmission of pressures across the elbow joint. *The Anatomical Record*, **150**, 243–7. https://doi.org/10.1002/ar.1091500305

[14] Smithson, K., Smith, J., Hogue, W., Mannen, E. and Ahmadi, S. (2020) Biomechanics of axial load transmission across the native human elbow. *Shoulder & Elbow*, **13**, 671–6. https://doi.org/10.1177/1758573220961025

[15] Hwang, J.T., Kim, Y., Bachman, D.R., Shields, M.N., Berglund, L.J., Fitzsimmons, A.T. et al. (2018) Axial load transmission through the elbow during forearm rotation. *Journal of Shoulder and Elbow Surgery*, Elsevier Inc. **27**, 530–7. https://doi.org/10.1016/j.jse.2017.10.003

[16] Wapler, C., Fontaine, C., Mesnil, P. and Chantelot, C. (2016) Medial collateral ligament healing after posttraumatic radial head arthroplasty: A retrospective study of 33 cases with a mean follow-up of 73 months. *Hand Surgery and Rehabilitation*, **35**, 44–50. https://doi.org/10.1016/j.hansur.2015.12.005

[17]   Tarassoli, P., McCann, P. and Amirfeyz, R. (2017) Complex instability of the elbow. *Injury*, **48**, 568–77. https://doi.org/10.1016/j.injury.2013.09.032

[18]   Seijas, R., Ares-Rodriguez, O., Orellana, A., Albareda, D., Collado, D. and Llusa, M. (2009) Terrible Triad of the Elbow. *Journal of Orthopaedic Surgery*, **17**, 335–9. https://doi.org/10.1177/230949900901700319

[19]   Najd Mazhar, F., Jafari, D. and Mirzaei, A. (2017) Evaluation of functional outcome after nonsurgical management of terrible triad injuries of the elbow. *Journal of Shoulder and Elbow Surgery*, **26**, 1342–7. https://doi.org/10.1016/j.jse.2017.05.012

[20]   Hou, F., Liang, X., Fan, W., Zhao, F. and Li, D. (2021) Analysis of twenty-five cases of terrible triad injury of the elbow surgically treated with a single lateral approach. *International Orthopaedics*, **45**, 241–6. https://doi.org/10.1007/s00264-020-04891-5

[21]   Beingessner, D.M., Pollock, J.W. and King, G.J.W. (2015) Elbow Fractures and Dislocations. In: Court-Brown CM, Heckman JD, McQueen MM, Ricci WM, and Tornetta III P, editors. *Rockwood and Green's Fractures in Adults*, 8th ed. Wolters Kluwer Health, Philadelphia. p. 1–23.

[22]   Rodriguez-Martin, J., Pretell-Mazzini, J., Andres-Esteban, E.M. and Larrainzar-Garijo, R. (2011) Outcomes after terrible triads of the elbow treated with the current surgical protocols. A review. *International Orthopaedics*, **35**, 851–60. https://doi.org/10.1007/s00264-010-1024-6

[23]   Jones, A.D.R. and Jordan, R.W. (2017) Complex Elbow Dislocations and the "Terrible Triad" Injury. *The Open Orthopaedics Journal*, **11**, 1394–404. https://doi.org/10.2174/1874325001711011394

[24]   Pugh, D.M.W., Wild, L.M., Schemitsch, E.H., King, G.J.W. and McKee, M.D. (2004) Standard Surgical Protocol to Treat Elbow Dislocations with Radial Head and Coronoid Fractures. *The Journal of Bone and Joint Surgery-American Volume*, **86**, 1122–30. https://doi.org/10.2106/00004623-200406000-00002

[25]   Forthman, C., Henket, M. and Ring, D.C. (2007) Elbow Dislocation With Intra-Articular Fracture: The Results of Operative Treatment Without Repair of the Medial Collateral Ligament. *The Journal of Hand Surgery*, **32**, 1200–9.

https://doi.org/10.1016/j.jhsa.2007.06.019

[26] Osborne, G. and Cotterill, P. (1966) Recurrent dislocation of the elbow. *The Journal of Bone and Joint Surgery British Volume*, **48**, 340–6. https://doi.org/10.1302/0301-620x.48b2.340

[27] Gupta, A., Barei, D., Khwaja, A. and Beingessner, D. (2014) Single-staged Treatment Using a Standardized Protocol Results in Functional Motion in the Majority of Patients With a Terrible Triad Elbow Injury. *Clinical Orthopaedics & Related Research*, **472**, 2075–83. https://doi.org/10.1007/s11999-014-3475-3

[28] Papatheodorou, L.K., Rubright, J.H., Heim, K.A., Weiser, R.W. and Sotereanos, D.G. (2014) Terrible triad injuries of the elbow: Does the coronoid always need to be fixed? *Clinical Orthopaedics and Related Research*, **472**, 2084–91. https://doi.org/10.1007/s11999-014-3471-7

[29] Ring, D., Jupiter, J.B. and Zilberfarb, J. (2002) Posterior dislocation of the elbow with fractures of the radial head and coronoid. *Journal of Bone and Joint Surgery*, **84**, 547–51. https://doi.org/10.2106/00004623-200204000-00006

[30] Jung, S.-W., Kim, D.-H., Kang, S.-H., Eho, Y.-J., Yang, S.-W. and Lee, G.-E. (2019) Risk Factors That Influence Subsequent Recurrent Instability in Terrible Triad Injury of the Elbow. *Journal of Orthopaedic Trauma*, **33**, 250–5. https://doi.org/10.1097/BOT.0000000000001425

[31] Lindenhovius, A.L.C., Jupiter, J.B. and Ring, D. (2008) Comparison of Acute Versus Subacute Treatment of Terrible Triad Injuries of the Elbow. 920–6. https://doi.org/10.1016/j.jhsa.2008.02.007

[32] Chemama, B., Bonnevialle, N., Peter, O., Mansat, P. and Bonnevialle, P. (2010) Terrible triad injury of the elbow: How to improve outcomes? *Orthopaedics & Traumatology: Surgery & Research*, **96**, 147–54. https://doi.org/10.1016/j.otsr.2009.11.009

[33] Jeong, W.-K., Oh, J.-K., Hwang, J.-H., Hwang, S.-M. and Lee, W.-S. (2010) Results of terrible triads in the elbow: the advantage of primary restoration of medial structure. *Journal of Orthopaedic Science*, **15**, 612–9. https://doi.org/10.1007/s00776-010-1515-8

[34] Chen, H., Shao, Y. and Li, S. (2019) Replacement or repair of terrible triad of the elbow.

Medicine, **98**, e13054. https://doi.org/10.1097/MD.000000000013054

[35] Watters, T.S., Garrigues, G.E., Ring, D. and Ruch, D.S. (2014) Fixation Versus Replacement of Radial Head in Terrible Triad: Is There a Difference in Elbow Stability and Prognosis? *Clinical Orthopaedics & Related Research*, **472**, 2128–35. https://doi.org/10.1007/s11999-013-3331-x

[36] Leigh, W.B. and Ball, C.M. (2012) Radial head reconstruction versus replacement in the treatment of terrible triad injuries of the elbow. *Journal of Shoulder and Elbow Surgery*, **21**, 1336–41. https://doi.org/10.1016/j.jse.2012.03.005

[37] Yan, M., Ni, J., Song, D., Ding, M., Liu, T. and Huang, J. (2015) Radial head replacement or repair for the terrible triad of the elbow: which procedure is better? *ANZ Journal of Surgery*, **85**, 644–8. https://doi.org/10.1111/ans.13060

[38] Chan, K., MacDermid, J.C., Faber, K.J., King, G.J.W. and Athwal, G.S. (2014) Can We Treat Select Terrible Triad Injuries Nonoperatively? *Clinical Orthopaedics & Related Research*, **472**, 2092–9. https://doi.org/10.1007/s11999-014-3518-9

[39] Pugh, D.M.W. and McKee, M.D. (2002) The "Terrible Triad" of the Elbow. *Techniques in Hand and Upper Extremity Surgery*, **6**, 21–9. https://doi.org/10.1097/00130911-200203000-00005

[40] Antoni, M., Eichler, D., Kempf, J.F. and Clavert, P. (2019) Anterior capsule re-attachment in terrible triad elbow injury with coronoid tip fracture. *Orthopaedics and Traumatology: Surgery and Research*,. https://doi.org/10.1016/j.otsr.2019.09.024

[41] Fern, S.E., Owen, J.R., Ordyna, N.J., Wayne, J.S. and Boardman, N.D. (2009) Complex varus elbow instability: A terrible triad model. *Journal of Shoulder and Elbow Surgery*, Elsevier Ltd. **18**, 269–74. https://doi.org/10.1016/j.jse.2008.10.022

[42] Fitzpatrick, M.J., Diltz, M., McGarry, M.H. and Lee, T.Q. (2012) A new fracture model for "terrible Triad" injuries of the elbow: Influence of forearm rotation on injury patterns. *Journal of Orthopaedic Trauma*, **26**, 591–6. https://doi.org/10.1097/BOT.0b013e31824135af

[43] Lanzerath, F., Knifka, J., Leschinger, T., Ott, N., Kahmann, S., Hackl, M. et al. (2022) The simulation of terrible triad injuries in fresh-frozen human cadaveric specimens with

intact soft tissue envelope. *Archives of Orthopaedic and Trauma Surgery*, **143**, 4229–37. https://doi.org/10.1007/s00402-022-04677-x

[44] Rhyou, I.H., Lee, J.H., Cho, C.-H., Park, S.-G., Lee, J.-H. and Kim, K.C. (2021) Patterns of injury mechanism observed in terrible triad. *Journal of Shoulder and Elbow Surgery*, **30**, e583–93. https://doi.org/10.1016/j.jse.2020.12.015

[45] Wake, H., Hashizume, H., Nishida, K., Inoue, H. and Nagayama, N. (2004) Biomechanical analysis of the mechanism of elbow fracture-dislocations by compression force. *Journal of Orthopaedic Science*, **9**, 44–50. https://doi.org/10.1007/s00776-003-0735-6

[46] Merz, B., Eckstein, F., Hillebrand, S. and Putz, R. (1997) Mechanical implications of humero-ulnar incongruity - Finite element analysis and experiment. *Journal of Biomechanics*, **30**, 713–21. https://doi.org/10.1016/S0021-9290(97)00014-6

[47] Renani, M.S., Rahman, M., Cil, A. and Stylianou, A.P. (2017) Ulna-humerus contact mechanics: Finite element analysis and experimental measurements using a tactile pressure sensor. *Medical Engineering and Physics*, Elsevier Ltd. **50**, 22–8. https://doi.org/10.1016/j.medengphy.2017.08.010

[48] Langohr, G.D.G., Willing, R., Medley, J.B., King, G.J.W. and Johnson, J.A. (2015) Contact analysis of the native radiocapitellar joint compared with axisymmetric and nonaxisymmetric radial head hemiarthroplasty. *Journal of Shoulder and Elbow Surgery*, Elsevier Ltd. **24**, 787–95. https://doi.org/10.1016/j.jse.2014.12.011

[49] Mellema, J.J., Doornberg, J.N., Dyer, G.S.M. and Ring, D. (2014) Distribution of Coronoid Fracture Lines by Specific Patterns of Traumatic Elbow Instability. *The Journal of Hand Surgery*, Elsevier Inc. **39**, 2041–6. https://doi.org/10.1016/j.jhsa.2014.06.123

[50] Mellema, J.J., Eygendaal, D., van Dijk, C.N., Ring, D. and Doornberg, J.N. (2016) Fracture mapping of displaced partial articular fractures of the radial head. *Journal of Shoulder and Elbow Surgery*, Elsevier Inc. **25**, 1509–16. https://doi.org/10.1016/j.jse.2016.01.030

[51] Fornalski, S., Gupta, R. and Lee, T.Q. (2003) Anatomy and Biomechanics of the Elbow

Joint. *Sports Medicine and Arthroscopy Review*, **11**, 1–9.

[52]   Bozon, O., Chrosciany, S., Loisel, M., Dellestable, A., Gubbiotti, L., Dumartinet-Gibaud, R. et al. (2022) Terrible triad injury of the elbow: a historical perspective. *International Orthopaedics*, Springer Berlin Heidelberg. https://doi.org/10.1007/s00264-022-05472-4

[53]   Stylianou, A. (2021) Computational approaches to study elbow biomechanics. *Annals of Joint*, **6**, 11–11. https://doi.org/10.21037/aoj.2020.04.01

[54]   Osawa, T., Moriyama, S. and Tanaka, M. (2014) Finite element analysis of hip joint cartilage reproduced from real bone surface geometry based on 3D-CT image. *Journal of Biomechanical Science and Engineering*, **9**, 1–8. https://doi.org/10.1299/jbse.13-00164

[55]   Anderson, A.E., Ellis, B.J., Maas, S.A., Peters, C.L. and Weiss, J.A. (2008) Validation of Finite Element Predictions of Cartilage Contact Pressure in the Human Hip Joint. *Journal of Biomechanical Engineering*, **130**. https://doi.org/10.1115/1.2953472

[56]   Li, M., Venäläinen, M.S., Chandra, S.S., Patel, R., Fripp, J., Engstrom, C. et al. (2021) Discrete element and finite element methods provide similar estimations for hip joint contact mechanics during walking gait. *Journal of Biomechanics*, Elsevier Ltd. **115**, 110163. https://doi.org/10.1016/j.jbiomech.2020.110163

[57]   Peña, E., Calvo, B., Martínez, M.A. and Doblaré, M. (2006) A three-dimensional finite element analysis of the combined behavior of ligaments and menisci in the healthy human knee joint. *Journal of Biomechanics*, **39**, 1686–701. https://doi.org/10.1016/j.jbiomech.2005.04.030

[58]   Haut Donahue, T.L., Hull, M.L., Rashid, M.M. and Jacobs, C.R. (2002) A Finite Element Model of the Human Knee Joint for the Study of Tibio-Femoral Contact. *Journal of Biomechanical Engineering*, **124**, 273–80. https://doi.org/10.1115/1.1470171

[59]   Mononen, M.E., Jurvelin, J.S. and Korhonen, R.K. (2013) Effects of radial tears and partial meniscectomy of lateral meniscus on the knee joint mechanics during the stance phase of the gait cycle - A 3D finite element study. *Journal of Orthopaedic Research*, **31**, 1208–17. https://doi.org/10.1002/jor.22358

[60] Chadwick, E.K.J. and Nicol, A.C. (2000) Elbow and wrist joint contact forces during occupational pick and place activities. *Journal of Biomechanics*, **33**, 591–600. https://doi.org/10.1016/S0021-9290(99)00184-0

[61] Safran, M., Ahmad, C.S. and Elattrache, N.S. (2005) Ulnar collateral ligament of the elbow. *Arthroscopy - Journal of Arthroscopic and Related Surgery*, **21**, 1381–95. https://doi.org/10.1016/j.arthro.2005.07.001

[62] An, K.N., Kwak, B.M., Chao, E.Y. and Morrey, B.F. (1984) Determination of muscle and joint forces: A new technique to solve the indeterminate problem. *Journal of Biomechanical Engineering*, **106**, 364–7. https://doi.org/10.1115/1.3138507

[63] Jansson, K.S., Michalski, M.P., Smith, S.D., LaPrade, R.F. and Wijdicks, C.A. (2013) Tekscan pressure sensor output changes in the presence of liquid exposure. *Journal of Biomechanics*, Elsevier. **46**, 612–4. https://doi.org/10.1016/j.jbiomech.2012.09.033

[64] Brimacombe, J.M., Wilson, D.R., Hodgson, A.J., Ho, K.C.T. and Anglin, C. (2009) Effect of calibration method on Tekscan sensor accuracy. *Journal of Biomechanical Engineering*, **131**, 1–4. https://doi.org/10.1115/1.3005165

[65] ABAQUS. (2013) ABAQUS 6.11 User's documentation. **IV**, 1100.

[66] Keyak, J.H., Kaneko, T.S., Tehranzadeh, J. and Skinner, H.B. (2005) Predicting proximal femoral strength using structural engineering models. *Clinical Orthopaedics and Related Research*, 219–28. https://doi.org/10.1097/01.blo.0000164400.37905.22

[67] Pellikaan, P., Giarmatzis, G., Vander Sloten, J., Verschueren, S. and Jonkers, I. (2018) Ranking of osteogenic potential of physical exercises in postmenopausal women based on femoral neck strains. Garcia Aznar JM, editor. *PLOS ONE*, **13**, e0195463. https://doi.org/10.1371/journal.pone.0195463

[68] Abel, A., Kahmann, S.L., Mellon, S., Staat, M. and Jung, A. (2020) An open-source tool for the validation of finite element models using three-dimensional full-field measurements. *Medical Engineering and Physics*, **77**. https://doi.org/10.1016/j.medengphy.2019.10.015

[69] Puth, M.-T., Neuhäuser, M. and Ruxton, G.D. (2015) On the variety of methods for calculating confidence intervals by bootstrapping. Childs D, editor. *Journal of Animal*

Ecology, **84**, 892–7. https://doi.org/10.1111/1365-2656.12382

[70] Cohen, J. (1977) Statistical Power Analysis for the Behavioral Sciences. 2nd ed. Elsevier. https://doi.org/10.1016/C2013-0-10517-X

[71] Pike, J.M., Athwal, G.S., Faber, K.J. and King, G.J.W. (2009) Radial Head Fractures-An Update. *Journal of Hand Surgery*, Elsevier Inc. **34**, 557–65. https://doi.org/10.1016/j.jhsa.2008.12.024

[72] Kaas, L., Van Riet, R.P., Vroemen, J.P.A.M. and Eygendaal, D. (2008) The incidence of associated fractures of the upper limb in fractures of the radial head. *Strategies in Trauma and Limb Reconstruction*, **3**, 71–4. https://doi.org/10.1007/s11751-008-0038-8

[73] Viceconti, M., Juarez, M.A., Curreli, C., Pennisi, M., Russo, G. and Pappalardo, F. (2020) Credibility of In Silico Trial Technologies—A Theoretical Framing. *IEEE Journal of Biomedical and Health Informatics*, **24**, 4–13. https://doi.org/10.1109/JBHI.2019.2949888

[74] Troy, K.L. and Grabiner, M.D. (2007) Off-axis loads cause failure of the distal radius at lower magnitudes than axial loads: A finite element analysis. *Journal of Biomechanics*, **40**, 1670–5. https://doi.org/10.1016/j.jbiomech.2007.01.018

[75] Oefner, C., Herrmann, S., Kebbach, M., Lange, H.E., Kluess, D. and Woiczinski, M. (2021) Reporting checklist for verification and validation of finite element analysis in orthopedic and trauma biomechanics. *Medical Engineering and Physics*, Elsevier Ltd. **92**, 25–32. https://doi.org/10.1016/j.medengphy.2021.03.011

[76] Yao, X., Zhou, K., Lv, B., Wang, L., Xie, J., Fu, X. et al. (2020) 3D mapping and classification of tibial plateau fractures. *Bone and Joint Research*, **9**, 258–67. https://doi.org/10.1302/2046-3758.96.BJR-2019-0382.R2

[77] Xie, X., Zhan, Y., Wang, Y., Lucas, J.F., Zhang, Y. and Luo, C. (2020) Comparative Analysis of Mechanism-Associated 3-Dimensional Tibial Plateau Fracture Patterns. *Journal of Bone and Joint Surgery*, **102**, 410–8. https://doi.org/10.2106/JBJS.19.00485

[78] Zhang, X., Zhang, Y., Fan, J., Yuan, F., Tang, Q. and Xian, C.J. (2019) Analyses of fracture line distribution in intra - articular distal radius fractures. *La Radiologia Medica*, Springer Milan. https://doi.org/10.1007/s11547-019-01025-9

[79] Li, S., Zhang, Y., Wang, G.-H., Li, K., Wang, J. and Ni, M. (2020) Melone's concept revisited in comminuted distal radius fractures: the three-dimensional CT mapping. *Journal of Orthopaedic Surgery and Research*, Journal of Orthopaedic Surgery and Research. **15**, 222. https://doi.org/10.1186/s13018-020-01739-x

[80] Zhang, Y., Sun, Y., Liao, S. and Chang, S. (2020) Three-Dimensional Mapping of Medial Wall in Unstable Pertrochanteric Fractures. *BioMed Research International*, **2020**, 1–8. https://doi.org/10.1155/2020/8428407

[81] Yimam, H.M., Dey, R., Rachuene, P.A., Kauta, N.J., Roche, S.J.L. and Sivarasu, S. (2022) Identification of recurring scapular fracture patterns using 3-dimensional computerized fracture mapping. *Journal of Shoulder and Elbow Surgery*, American Shoulder and Elbow Surgeons. **31**, 571–9. https://doi.org/10.1016/j.jse.2021.08.036

[82] Wang, C., Zhu, Y., Long, H., Lin, Z., Zhao, R., Sun, B. et al. (2021) Three-dimensional mapping of distal humerus fracture. *Journal of Orthopaedic Surgery and Research*, **16**, 545. https://doi.org/10.1186/s13018-021-02691-0

[83] Cho, J.-W., Yang, Z., Lim, E.J., Sakong, S., Choi, W., Son, W.S. et al. (2021) Multifragmentary patellar fracture has a distinct fracture pattern which makes coronal split, inferior pole, or satellite fragments. *Scientific Reports*, Nature Publishing Group UK. **11**, 22836. https://doi.org/10.1038/s41598-021-02215-0

[84] Armitage, B.M., Wijdicks, C.A., Tarkin, I.S., Schroder, L.K., Marek, D.J., Zlowodzki, M. et al. (2009) Mapping of Scapular Fractures with Three-Dimensional Computed Tomography. *The Journal of Bone and Joint Surgery-American Volume*, **91**, 2222–8. https://doi.org/10.2106/JBJS.H.00881

[85] Cole, P.A., Mehrle, R.K., Bhandari, M. and Zlowodzki, M. (2013) The Pilon Map. *Journal of Orthopaedic Trauma*, **27**, e152–6. https://doi.org/10.1097/BOT.0b013e318288a7e9

[86] Molenaars, R.J., Mellema, J.J., Doornberg, J.N. and Kloen, P. (2015) Tibial Plateau Fracture Characteristics: Computed Tomography Mapping of Lateral, Medial, and Bicondylar Fractures. *Journal of Bone and Joint Surgery*, **97**, 1512–20. https://doi.org/10.2106/JBJS.N.00866

[87] Chen, P., Shen, H., Wang, W., Ni, B., Fan, Z. and Lu, H. (2016) The morphological features of different Schatzker types of tibial plateau fractures: a three-dimensional computed tomography study. *Journal of Orthopaedic Surgery and Research*, **11**, 94. https://doi.org/10.1186/s13018-016-0427-5

[88] Krause, M., Preiss, A., Müller, G., Madert, J., Fehske, K., Neumann, M. V et al. (2016) Intra-articular tibial plateau fracture characteristics according to the "Ten segment classification." *Injury*, Elsevier Ltd. **47**, 2551–7. https://doi.org/10.1016/j.injury.2016.09.014

[89] Dugarte, A.J., Tkany, L., Schroder, L.K., Petersik, A. and Cole, P.A. (2017) Comparison of 2 versus 3 dimensional fracture mapping strategies for 3 dimensional computerized tomography reconstructions of scapula neck and body fractures. *Journal of Orthopaedic Research*, 265–71. https://doi.org/10.1002/jor.23603

[90] Hasan, A.P., Phadnis, J., Jaarsma, R.L. and Bain, G.I. (2017) Fracture line morphology of complex proximal humeral fractures. *Journal of Shoulder and Elbow Surgery*, Elsevier Inc. **26**, e300–8. https://doi.org/10.1016/j.jse.2017.05.014

[91] Xie, X., Zhan, Y., Dong, M., He, Q., Lucas, J.F., Zhang, Y. et al. (2017) Two and Three-Dimensional CT Mapping of Hoffa Fractures. *Journal of Bone and Joint Surgery*, **99**, 1866–74. https://doi.org/10.2106/JBJS.17.00473

[92] Kfuri, M. and Schatzker, J. (2018) Revisiting the Schatzker classification of tibial plateau fractures. *Injury*, Elsevier Ltd. **49**, 2252–63. https://doi.org/10.1016/j.injury.2018.11.010

[93] Fürnstahl, P., Székely, G., Gerber, C., Hodler, J., Snedeker, J.G. and Harders, M. (2012) Computer assisted reconstruction of complex proximal humerus fractures for preoperative planning. *Medical Image Analysis*, **16**, 704–20. https://doi.org/10.1016/j.media.2010.07.012

[94] Vlachopoulos, L., Székely, G., Gerber, C. and Fürnstahl, P. (2018) A scale-space curvature matching algorithm for the reconstruction of complex proximal humeral fractures. *Medical Image Analysis*, Elsevier B.V. **43**, 142–56. https://doi.org/10.1016/j.media.2017.10.006

[95] Amberg, B., Romdhani, S. and Vetter, T. (2007) Optimal step nonrigid ICP algorithms

for surface registration. *Proceedings of the IEEE Computer Society Conference on Computer Vision and Pattern Recognition,*. https://doi.org/10.1109/CVPR.2007.383165

[96]   Golub, G.H. and Van Loan, C.F. (2013) Chapter 5: Orthogonalization and Least Squares. *Matrix Computations*, 4th ed. The Johns Hopkins University Press, Baltimore. p. 233–302.

[97]   Codman, E.A. (1934) Fractures in relation to the subacromial bursa. In: Todd T, editor. *The Shoulder, Rupture of the Supraspinatus Tendon and Other Lesions in or about the Subacromial Bursa*, Boston, MA. p. 313–31.

[98]   Carofino, B.C. and Leopold, S.S. (2013) Classifications in brief: The neer classification for proximal humerus fractures. *Clinical Orthopaedics and Related Research*, **471**, 39–43. https://doi.org/10.1007/s11999-012-2454-9

[99]   Majed, A., Macleod, I., Bull, A.M.J., Zyto, K., Resch, H., Hertel, R. et al. (2011) Proximal humeral fracture classification systems revisited. *Journal of Shoulder and Elbow Surgery*, **20**, 1125–32. https://doi.org/10.1016/j.jse.2011.01.020

[100]   Dahan, G., Trabelsi, N., Safran, O. and Yosibash, Z. (2016) Verified and validated finite element analyses of humeri. *Journal of Biomechanics*, Elsevier. **49**, 1094–102. https://doi.org/10.1016/j.jbiomech.2016.02.036

[101]   Brown, C.P., Nguyen, T.C., Moody, H.R., Crawford, R.W. and Oloyede, A. (2009) Assessment of common hyperelastic constitutive equations for describing normal and osteoarthritic articular cartilage. *Proceedings of the Institution of Mechanical Engineers, Part H: Journal of Engineering in Medicine*, **223**, 643–52. https://doi.org/10.1243/09544119JEIM546

[102]   Armah, S.K. (2018) Stress Analysis of an Artificial Human Elbow Joint: Application of Finite Element Analysis. *American Journal of Engineering and Applied Sciences*, **11**, 1–18. https://doi.org/10.3844/ajeassp.2018.1.18

[103]   Yeh, O.C. and Keaveny, T.M. (2001) Relative roles of microdamage and microfracture in the mechanical behavior of trabecular bone. *Journal of Orthopaedic Research*, **19**, 1001–7. https://doi.org/10.1016/S0736-0266(01)00053-5

[104]   Nalla, R.K., Kinney, J.H. and Ritchie, R.O. (2003) Mechanistic fracture criteria for the

failure of human cortical bone. *Nature Materials*, **2**, 164–8. https://doi.org/10.1038/nmat832

[105] Langerhuizen, D.W.G., Janssen, S.J., Mallee, W.H., van den Bekerom, M.P.J., Ring, D., Kerkhoffs, G.M.M.J. et al. (2019) What Are the Applications and Limitations of Artificial Intelligence for Fracture Detection and Classification in Orthopaedic Trauma Imaging? A Systematic Review. *Clinical Orthopaedics & Related Research*, **477**, 2482–91. https://doi.org/10.1097/CORR.0000000000000848

[106] Chung, S.W., Han, S.S., Lee, J.W., Oh, K.-S., Kim, N.R., Yoon, J.P. et al. (2018) Automated detection and classification of the proximal humerus fracture by using deep learning algorithm. *Acta Orthopaedica*, **89**, 468–73. https://doi.org/10.1080/17453674.2018.1453714

[107] de Marinis, R., Marigi, E.M., Atwan, Y., Yang, L., Oeding, J.F., Gupta, P. et al. (2023) Current clinical applications of artificial intelligence in shoulder surgery: what the busy shoulder surgeon needs to know and what's coming next. *JSES Reviews, Reports, and Techniques*, **3**, 447–53. https://doi.org/10.1016/j.xrrt.2023.07.008

[108] Kuo, R.Y.L., Harrison, C., Curran, T.-A., Jones, B., Freethy, A., Cussons, D. et al. (2022) Artificial Intelligence in Fracture Detection: A Systematic Review and Meta-Analysis. *Radiology*, **304**, 50–62. https://doi.org/10.1148/radiol.211785

Curriculum Vitae

Personal Data

Name	Stephanie Lucina Kahmann
Nationality	German
Date of birth	December 16th, 1992
Place of birth	Münster, Germany

Education

2018-2024	PhD candidate at the Biomechanics Laboratory, Center for Orthopedic and Trauma Surgery, University of Cologne
2015-2018	Master of Science in Biomedical Engineering, FH Aachen, Jülich, Germany (final grade: 1.1)
2012-2015	Bachelor of Engineering in Biomedical Engineering, FH Aachen, Jülich, Germany (final grade: 1.6)

Experience

Professional	Junior Design Engineer for spinal systems on the US market
Research	Biomechanical cadaver testing and computational modeling of different anatomical sites
Leading	Supervising students in their Bachelor's and Master's thesis
	Coordinating contract research with industrial partners

International Experience

01/2020-02/2020: Research Stay at Division of Biomechanics (BMe), Mechanical Engineering, KU Leuven, Belgium

07/2019: Research Stay at Division of Macroscopic and Clinical Anatomy, Gottfried Schatz Research Center, Medical University of Graz, Graz, Austria

06/2017-08/2017: Research Project at Oxford Orthopaedic Engineering Centre (OOEC), NDORMS, University of Oxford, Oxford, United Kingdom

Scholarships

06/2018

ECCOMAS Mobility Scholarship for attending the 6th Conference on Computational Mechanics, Glasgow, United Kingdom, June 11-15th, 2018

06/2017-08-2017

Erasmus+ Internship Grant for Research Project at Oxford University

09/2016-08/2017

German Scholarship "Deutschlandstipendium" of Federal Ministry for Education and Research, and FH Aachen

Publications

Articles in international reviewed journals

Kahmann, S.L., Sas, A., Große Hokamp, N., van Lenthe, G. H., Müller, L.-P., Wegmann, K., 2023. A combined experimental and finite element analysis of the human elbow under loads of daily living. J. Biomech. 158, 111766. https://doi.org/10.1016/j.jbiomech.2023.111766

Kahmann, S.L., Rausch, V., Plümer, J., Müller, L.-P., Pieper, M., Wegmann, K., 2022. The automized fracture edge detection and generation of three-dimensional fracture probability heat maps. Med. Eng. Phys. 110, 103913. https://doi.org/10.1016/j.medengphy.2022.103913

Lanzerath F, Knifka J, Leschinger T, Ott N, **Kahmann S**, Hackl M, Müller LP, Wegmann K, 2023. The simulation of terrible triad injuries in fresh-frozen human cadaveric specimens with intact soft tissue envelope. Arch. Orthop. Trauma Surg. 143, 4229-4237. https://doi.org/10.1007/s00402-022-04677-x.

Lenz M, **Kahmann S**, Behbahani M, Pennig L, Hackl M, Leschinger T, Müller LP, Wegmann K. 2023. Influence of rotator cuff preload on fracture configuration in proximal humerus fractures: a proof of concept for fracture simulation. Arch. Orthop. Trauma Surg. 143, 2467-2474. https://doi.org/10.1007/s00402-022-04471-9

Ott N, **Kahmann S**, Hackl M, Uschok S, Peter Müller L, Wegmann K. 2021. The effect of metaglene lateralization on joint mobility of reverse shoulder arthroplasty: A cadaveric biomechanical study. J. Orthop. 24, 9-14. https://doi.org/10.1016/j.jor.2021.02.016

Rausch V, Harbrecht A, **Kahmann SL**, Fenten T, Jovanovic N, Hackl M, Müller LP, Staat M, Wegmann K. 2020. Osteosynthesis of Phalangeal Fractures: Biomechanical Comparison of

Kirschner Wires, Plates, and Compression Screws. J. Hand. Surg. Am. 45, 987.e1-987.e8. https://doi.org/10.1016/j.jhsa.2020.04.010

Rausch V, **Kahmann SL**, Baltschun C, Staat M, Müller LP, Wegmann K. 2020. Pressure Distribution to the Distal Biceps Tendon at the Radial Tuberosity: A Biomechanical Study. J. Hand. Surg. Am. 45, 776.e1-776.e9. https://doi.org/10.1016/j.jhsa.2020.01.006

Abel A, **Kahmann SL**, Mellon S, Staat M, Jung A. 2019. An open-source tool for the validation of finite element models using three-dimensional full-field measurements. Med. Eng. Phys. 77, 125-129. https://doi.org/10.1016/j.medengphy.2019.10.015.

Hackl M, Wegmann K, **Kahmann SL**, Heinze N, Staat M, Neiss WF, Scaal M, Müller LP. 2017. Reply to the letter to the editor: shortening osteotomy of the proximal radius. Knee Surg. Sports Traumatol. Arthrosc. 25, 3328-3329. https://doi.org/10.1007/s00167-017-4666-8.

Hackl M, Wegmann K, **Kahmann SL**, Heinze N, Staat M, Neiss WF, Scaal M, Müller LP. 2017. Radial shortening osteotomy reduces radiocapitellar contact pressures while preserving valgus stability of the elbow. Knee Surg. Sports Traumatol. Arthrosc. 25, 2280-2288. https://doi.org/10.1007/s00167-017-4468-z.

Articles submitted to or in preparation for international reviewed journals

[In Press] Wegmann, S.*, **Kahmann, S.L.***, Marchal, C., Leschinger, T., Wegmann, K. Müller, L.-P., Hackl, M., 2024. Biomechanical differences between a wide and narrow box-shaped reconstruction using the long head of biceps tendon in superior capsular reconstruction for irreparable supraspinatus tendon tears. J. Shoulder Elb. Surg. https://doi.org/10.1016/j.jse.2024.05.040
*Contributed equally

[Accepted] Krane, F., Wegmann, K., Schlender, J.F., **Kahmann, S.L.**, Harbrecht, A., Müller L.P., Leschinger, T. The temperature profile in elbow arthroscopy under radiofrequency ablation. Arthroscopy

[Submitted] Pucher, C., Lanzerath, F., **Kahmann, S.L.**, Hackl, M., Evaluation of the interposition arthtroplasty of the elbow by means of intraarticular contact pressure and joint mechanics.

[In Preparation] **Kahmann, S.L.***, Ott, N.*, Denk, A., Müller, L.-P., Wegmann, K. The dorsal fenestration at the proximal ulna in revision prosthetics – a biomechanical weak spot? A biomechanical study and finite element analysis. *Contributed equally

[In Preparation] **Kahmann, S.L.**, Denk, A., Harbrecht, A., Müller, L.-P., Wegmann, K. Prototype versus common locking screws in proximal humerus fracture fixations: a finite element analysis and cadaveric biomechanical study.

[In Preparation] Plümer, J., Rausch, V., **Kahmann, S.L.**, Hackl, M., Schildhauer, T.M., Müller, L.-P., Wegmann, K. Humeral head fracture fragment dislocation using a four-part main fragment fracture model.

[In Preparation] Uschok, S., Leschinger, T., **Kahmann, S.L.**, Hackl, M., Watts, A., Müller, L.-P., Wegmann, K. Tension band wiring versus suture repair in simple, transverse olecranon fractures: a cadaver model.

[In Preparation] **Kahmann, S.L.***, Rausch, V.*, Garajova, L., Comes, J.N., Terstegge, L., Gubaidullin, G., Müller, L.-P., Wegmann, K. The instantaneous center of rotation of the elbow. *Contributed equally

[In Preparation] Rausch, V., **Kahmann, S.L.**, Chen, X., Müller, L.-P., Wegmann, K. Triceps stiffness following off-loading sutures after olecranon fractures: a biomechanical analysis.

Eidesstattliche Erklärung

Hiermit versichere ich an Eides statt, dass ich die vorliegende Dissertationsschrift selbstständig und ohne die Benutzung anderer als der angegebenen Hilfsmittel angefertigt habe. Alle Stellen - einschließlich Tabellen, Karten und Abbildungen -, die wörtlich oder sinngemäß aus veröffentlichten und nicht veröffentlichten anderen Werken im Wortlaut oder dem Sinn nach entnommen sind, sind in jedem Einzelfall als Entlehnung kenntlich gemacht. Ich versichere an Eides statt, dass diese Dissertationsschrift noch keiner anderen Fakultät oder Universität zur Prüfung vorgelegen hat; dass sie - abgesehen von unten angegebenen Teilpublikationen - noch nicht veröffentlicht worden ist sowie, dass ich eine solche Veröffentlichung vor Abschluss der Promotion nicht ohne Genehmigung der / des Vorsitzenden des IPHS-Promotionsausschusses vornehmen werde. Die Bestimmungen dieser Ordnung sind mir bekannt. Die von mir vorgelegte Dissertation ist von Prof. Dr. med. Kilian Wegmann betreut worden.

Darüber hinaus erkläre ich hiermit, dass ich die Ordnung zur Sicherung guter wissenschaftlicher Praxis und zum Umgang mit wissenschaftlichem Fehlverhalten der Universität zu Köln gelesen und sie bei der Durchführung der Dissertation beachtet habe und verpflichte mich hiermit, die dort genannten Vorgaben bei allen wissenschaftlichen Tätigkeiten zu beachten und umzusetzen.

Übersicht der Publikationen

Kahmann, S.L., Sas, A., Große Hokamp, N., van Lenthe, G. H., Müller, L.-P., Wegmann, K., 2023. A combined experimental and finite element analysis of the human elbow under loads of daily living. J. Biomech. 158, 111766. https://doi.org/10.1016/j.jbiomech.2023.111766

Kahmann, S.L., Rausch, V., Plümer, J., Müller, L.-P., Pieper, M., Wegmann, K., 2022. The automized fracture edge detection and generation of three-dimensional fracture probability heat maps. Med. Eng. Phys. 110, 103913. https://doi.org/10.1016/j.medengphy.2022.103913

Ich versichere, dass ich alle Angaben wahrheitsgemäß nach bestem Wissen und Gewissen gemacht habe und verpflichte mich, jedmögliche, die obigen Angaben betreffenden Veränderungen, dem IPHS-Promotionsausschuss unverzüglich mitzuteilen.

29.07.2024   Stephanie Kahmann